Hydro-morphodynamic modelling of mangroves imposed by tidal waves using finite element discontinuous Galerkin method

Fanous, M., Daneshkhah, A., Eden, J. M., Remesan, R. & Palade, V

Hydro-morphodynamic modelling of mangroves imposed by tidal waves using finite element discontinuous Galerkin method

Majdi Fanous [a,*], Alireza Daneshkhah [a], Jonathan M. Eden [b], Renji Remesan [c], Vasile Palade [a]

[a] *Centre for Computational Science & Mathematical Modelling, Coventry University, Priory Street, Coventry, CV1 5FB, United Kingdom*
[b] *Centre for Agroecology, Water and Resilience, Coventry University, Ryton Gardens, Wolston Lane, Warwickshire, CV8 3LG, United Kingdom*
[c] *School of Water Resources, Indian Institute of Technology Kharagpur, Kharagpur, West Bengal, 721302, India*

A B S T R A C T

Modelling the hydro-morphodynamics of mangrove environments is key for implementing successful protection and restoration projects in a climatically vulnerable region. Nevertheless, simulating such dynamics is faced with computational and time complexities, given the nonlinear and complex nature of the problem, which could become a bottleneck for large-scale applications. This study investigates the effect of mangrove environments on the hydro-morphodynamics of its region. A depth-averaged model was built using a novel finite element model for simulating coastal models, within *Thetis*. The Sundarbans, the largest mangrove forest in the world located between India and Bangladesh, is taken as a case study. The Sundarbans is regularly subjected to tropical cyclones, the impacts of which endanger the lives of the region's four million people. This is a first-time application of a coupled hydro-morphodynamic model using discontinuous Galerkin finite element discretisation for modelling mangrove environments in a real-world application. A wetting drying scheme was implemented in the models in order to avoid numerical instabilities. The effect of mangrove environments is demonstrated, by imposing periodic tidal boundary conditions using TPXO tidal solver, using experiments with and without mangroves. The model is validated against the results of another study on the same region and tidal gauge data. Mangrove environments are able to decrease water elevations and velocities by more than 97%, and prevent almost any sediment erosion when compared with the experiment with no mangroves.

1. Introduction

According to the World Meteorological Society (WMO) Secretary General Professor Petteri Taalas, at the current rate of greenhouse gas emissions, the increase in temperature will far exceed 1.5 °C to 2 °C above pre-industrial levels (World Meteorological Organization, 2021). Such rise in temperature has increased the loss of ice glaciers, which in turn increased sea-level rise from 3.3 mm per year, between 2006 and 2015, to 4.4 mm in recent years (World Meteorological Organization, 2021). As the sea level rises, it is predicted that 268–286 million people could be at risk of coastal flooding by 2030, with the number increasing to up to 411 million people by 2060. In addition to flooding, the rise in sea level is also increasing erosion rates, thus imposing threats to people living at the coast. However, in areas where natural wetlands are present, such as mangrove trees, it has been noticed that erosion rates are negligible and surge levels have decreased. This makes the protection and restoration projects of mangroves a vital strategy for climate change mitigation as was specified in the Second Working Group contribution to the Sixth Assessment Report (AR6) of the Intergovernmental Panel on Climate Change (IPCC_AR6_WGII) Climate Change 2022: Impacts, Adaptation and Vulnerability" (Masson-Delmote et al., 2022).

The implementation of a proper restoration or protection project requires a robust numerical model to simulate responses to different climatic stressors i.e. high waves, sea level rise, cyclones. Nonetheless, with the importance of such projects, there are several challenges, related to the numerical models, that could hinder their success. Put simply, the model should be accurate enough to properly simulate the given settings, continuously monitor change, and quantify mangroves capacity in attenuating waves and preventing erosion.

Building such a model requires solving the hydro-morphodynamics, which is computationally expensive, and such complexity can grow exponentially for large-scale problems. Nonetheless, solving those complex nonlinear relationships in the model is essential to properly implement climate change mitigation strategies. If these issues were not properly tackled, the ability to provide future predictions, about the success and sustainability of protection and restoration projects, would be less reliable and with high uncertainty.

Table 1
Software summary for different dimensions and discretisation methods.

Model	Dimension	Discretisation	Reference
MIKE 11	1D	FDM	Sholichin et al. (2017)
Cliffs	1D/2D	FDM	Tolkova (2014)
XBeach	1D/2D	FDM	Bolle et al. (2010)
COULWAVE	1D/2D	FDM	Lynett et al. (2004)
HEC-RAS	1D/2D	FDM/FVM	Alvarez et al. (2016)
FUNWAVE	1D/2D	FDM/FVM	Kennedy et al. (2000)
Celeris Base	2D	FDM/FVM	Tavakkol and Lynett (2020)
SWAN	2D	FDM	Ou et al. (2002)
MIKE 21	2D	FVM	Warren and Bach (1992)
ADCIRC	2D	FEM/FVM	Luettich and Westerink (2004)
NHWAVE	Q3D	FDM/FVM	Ma et al. (2012)
COMSIM	Q3D	FDM/FVM	Erduran and Kutija (2003)
Delft3D	2D/3D	FDM	Waldman et al. (2017)
TELEMAC 3D	2D/3D	FEM/FVM	Villaret et al. (2013)
ROMS	3D	FDM	Warner et al. (2008)
ECOMSED	3D	FDM	Harris et al. (2005)
MPAS-Ocean	3D	FVM	Ringler et al. (2013)

In terms of hydrodynamic and sediment transport applications, numerical modelling has been extensively applied because of its ability to simulate different conditions and its lower cost when compared with flume and in-situ experiments (Brand et al., 2020). Such models can be classified as 1D and usually utilised when time is the key element, although it does not capture all complex features present in a flow; 2D (or 2Dh), uses the nonlinear shallow water equations (NSWE) to capture more interactions between the waves and shoreline by averaging the main variables over the vertical; Boussinesq models that use Boussinesq equations to incorporate frequency dispersion; quasi-3D models that model velocity in vertical layers; 3D models which can capture more complex flow interactions than the 2D ones; and oceanographic-type models which simulate the physical state and dynamic properties of oceans (Sholichin et al., 2017; Warren and Bach, 1992; Tavakkol and Lynett, 2020; Ma et al., 2012; Waldman et al., 2017; Harris et al., 2005).

For these kind of problems, different discretisation methods could be applied, such as the finite difference method (FDM), finite volume method (FVM), and finite element method (FEM) (Prastica, 2018; Purohit et al., 2015; Peng, 2012). In addition, there exists a range of commercially available software that can solve hydrodynamic and sediment transport problems using the aforementioned discretisation methods and with different dimensions.

Table 1 provides examples of different software that solves hydrodynamic and sediment transport problems for different dimensions using different discretisation methods.

Although the capabilities and accuracy of these modelling approaches have been greatly improved when implemented in the software mentioned above, the main issue among such numerical models is their computational cost. In fact, there is always a trade-off between highly accurate, yet computationally expensive, models such as 3D models, and models that are not so accurate but are much faster such as the 1D models. Such issues become more prevalent when performing climate modelling analysis due to the large-scale spatial domains required to properly assess the region of study.

In addition, the discretisation method plays an important role in the accuracy-computational complexity dilemma. To explain, FDM-based discretisation methods are computationally the cheapest, however they face issues and difficulties when modelling complex geometries and meshes between imposing accurate boundary conditions and maintaining stability (Shu and Tan, 2017). The FVMs, on the other hand, have better accuracy and are often used for advection-dominated problems, although they are nominally only first-order accurate (Kärnä et al., 2018). Similar to FDM, FVM faces issues estimating the solutions around complex corners (Shchepetkin and McWilliams, 2003). Furthermore, the finite element methods for unstructured grid models, are based on the continuous Galerkin finite element (also known

as hybrid FE-FV) method like the Advanced Circulation Model (AD-CIRC) (Luettich and Westerink, 2004). Although these models provide better accuracy than FV models, they require stabilisation for advection problems and solving using a fully coupled system, which is less efficient in parallel computing applications (Kärnä et al., 2018). Other models have applied a discontinuous Galerkin (DG) finite element discretisation that is locally fully conservative, similar to FVM, but with a higher-order accuracy (Castillo and Gómez, 2021). This also helps in decreasing computational time by allowing for parallel computations.

Several research studies have been conducted in the field of modelling hydrodynamics and sediment transport in mangrove environments using numerical models (Wahid et al., 2007; Cannon et al., 2020; Le Minor et al., 2019). However, several limitations were present in such studies, such as using one-dimensional modelling (Wahid et al., 2007), using finite difference method (Cannon et al., 2020), and using a restricted or simplified spatial domain or region (Le Minor et al., 2019).

The aim of this work is to present a novel 2D depth-averaged model for both hydrodynamic and sediment transport processes for mangrove environments. This model is developed by appropriately adopting a FE-DG method for simulating coastal and estuarine flows (Kärnä et al., 2018); and is built on top of Firedrake, to create an automated system for solving partial differential equations (PDEs) using the FEM. To demonstrate its potential, we apply our approach to analyse the mangrove environments of the Sundarbans region, the largest mangrove ecosystem in the world. This work represents the first application of a hydro-morphodynamic model for a large and complex problem using the FE-DG method, to simulate the effect of vegetation on waves and sediment transport in both of its modes: bedload and suspended. We compare our model with Sindhu and Unnikrishnan (2013) based on the hydrodynamic performance of the models when compared with Paradip tidal gauge data. Our model achieved better accuracy especially in estimating peak tidal heights. We implement the proposed approach and related computations within Thetis.

This paper is organised as follows. In Section 2, we introduce the hydro-morphodynamic equations and some corrections done to avoid model instabilities and inaccuracies. In Section 3, we discuss the discontinuous Galerkin method in details and its form when solving for sediment transport and Exner equation. In Section 4, we present our case study with the constructed domain, mesh, and applied conditions. In Section 5, we discuss the results and demonstrate the effectiveness of mangrove environments in attenuating waves and preventing erosion through different experiments. Additionally, we performed a sensitivity analysis test on use of different values of the friction factors. In Section 6, we compare our results with another paper and with tidal data to validate our model's accuracy and robustness. Finally, in Section 7, we conclude our work and discuss present limitations and possible solutions.

2. Hydro-morphodynamic model

As stated above, the aim of this study is to introduce a novel 2D depth-averaged model for both hydrodynamic and sediment transport processes, or simply the hydro-morphodynamic model, for mangrove environments. Therefore, it is necessary to outline the set of equations required to model the hydro-morphodynamic process. The advantage of hydro-morphodynamic model is that it can simulate both suspended and bedload transport coupled with hydrodynamic movements. Notably, we used a 2D (2D depth-averaged model) instead of a 3D model due to the fact that the depth scale is much smaller than the horizontal in the Sundarbans region studied (less than 2.5 km deep and more than 1000 km wide). Furthermore, we have included a slope effect magnitude and angle corrections to account for any slope changes for the morphodynamics. With respect to the hydrodynamics, wave velocities in this region are very slow. Given that the Sundarbans region has an average of 80 km length (distance between the land and sea

extents of the mangroves), vertical gradients would not influence on the hydrodynamics.

We construct the aforementioned hydro-morphodynamic model for the large scale and complex problem (i.e., mangrove forest) by further developing the work of Clare et al. (2021) who developed a hydro-morphodynamic for a lab-based curved channel. By depth-averaging from the bed, z_b, to the water surface, η, the hydrodynamic equations of the 2D model are developed (Clare et al., 2021). With respect to the boundary conditions, a kinematic boundary condition is applied to the water surface as a free moving boundary, where the bed is assumed to be impermeable, i.e water does not pass through the bed. Therefore, the nonlinear shallow water equations used in this model are:

$$\frac{\partial \eta}{\partial t} + \nabla \cdot \left(h\overline{\mathbf{u}} \right) = 0, \tag{1}$$

$$\frac{\partial \overline{\mathbf{u}}}{\partial t} + \overline{\mathbf{u}} \cdot \nabla \overline{\mathbf{u}} - \nu \nabla^2 \overline{\mathbf{u}} + f\overline{\mathbf{u}}^{\perp} + g\nabla \eta = -\frac{\tau_b}{\rho h}, \tag{2}$$

$$\frac{\tau_b}{\rho} = gn^2 \frac{|\overline{\mathbf{u}}|\overline{\mathbf{u}}}{h^{\frac{1}{3}}}, \tag{3}$$

where $h = \eta - z_b$ is the depth, ν is the turbulent kinematic eddy viscosity, and $\overline{\mathbf{u}}$ is the depth-averaged velocity vector where its components, $\overline{\mathbf{u_1}}$ and $\overline{\mathbf{u_2}}$, represent flow in the x and y direction, respectively. The term $f\overline{\mathbf{u}}^{\perp}$ is the Coriolis "force", where $\overline{\mathbf{u}}^{\perp}$ is the velocity vector rotated counter-clockwise over 90° and $f = 2\Omega \sin(\zeta)$, in which Ω is the angular frequency of the Earth's rotation and ζ is latitude.

In Eq. (3), the seabed roughness is represented using the Manning's equation for bed shear stress τ_b using the Manning's coefficient n. A "wetting and drying" term is added to prevent the model from instability, when water depth becomes negative at the shore near the mangrove trees, according to the formulation of Kärnä et al. (2011). It should be noted that the wind effects were not included in the proposed model, since we are mainly concerned with tide effects on mangrove environments. Nonetheless, given access to the atmospheric forcing data of the selected region, the proposed model can be further developed to include wind effects, which is important to evaluate the impact of the extreme climatic events (e.g., cyclones) on the mangrove environments.

We take a Eulerian approach for solving the sediment equations instead of the Lagrangian approach. This is to reduce the computational complexity in solving the individual particles by taking the concentration of sediment particles and calculating sediment dynamics using an advection–diffusion equation. We split the model domain into bedload and suspended sediment zones with an interface $z = z_b + \delta^*$ where δ^* is the height of the bedload zone.

Applying the boundary condition, combining diffusion and dispersion effects, having a long sedimentation process, the depth-averaged sediment concentration becomes:

$$\frac{\partial}{\partial t}(h\bar{c}) + \frac{\partial}{\partial x}\left(h\overline{u_1 c}\right) + \frac{\partial}{\partial y}\left(h\overline{u_2 c}\right)$$
$$= \frac{\partial}{\partial x}\left[h\left(e_s \frac{\partial \bar{c}}{\partial x}\right)\right] + \frac{\partial}{\partial y}\left[h\left(e_s \frac{\partial \bar{c}}{\partial y}\right)\right] + E_b - D_b, \tag{4}$$

where $\bar{c}$ is the sediment concentration, e_s is the sediment turbulent diffusivity coefficient given by $e_s = \nu_s^h / \sigma_s$ in which ν_s^h is the horizontal viscosity and σ_s is the turbulent Schmidt number. E_b is the erosion flux, defined by the sediment gradient boundary condition as

$$E_b = -\left. e_s \frac{\partial c}{\partial z} \right|_{z=z_b} = w_s c_{b*}, \tag{5}$$

where w_s is the settling velocity of the sediment particles, and c_{b*} is the equilibrium near-bed sediment concentration; and the deposition flux, denoted by D_b, defined by the concentration boundary condition as

$$D_b = w_s c_b = \left. w_s c \right|_{z=z_b}, \tag{6}$$

where c_b is the actual sediment concentration at the bed.

It should be noted that the above equation is derived following standard practice, by assuming δ^* to be small, and the boundary condition is applied at the bed .

The main challenge in solving Eq. (4) is calculating $\overline{uc}$ due to the coupled nature of the hydrodynamic and sediment transport model. A solution for that would be to rewrite Eq. (4) as an advection–diffusion equation for $\bar{c}$ following (Huybrechts et al., 2010):

$$\frac{\partial}{\partial t}(h\bar{c}) + \frac{\partial}{\partial x}\left(hu_{\text{adv}_1}\bar{c}\right) + \frac{\partial}{\partial y}\left(hu_{\text{adv}_2}\bar{c}\right)$$
$$= \frac{\partial}{\partial x}\left[h\left(\epsilon_s \frac{\partial \bar{c}}{\partial x}\right)\right] + \frac{\partial}{\partial y}\left[h\left(\epsilon_s \frac{\partial \bar{c}}{\partial y}\right)\right] + E_b - D_b \tag{7}$$

with the advection velocity:

$$\mathbf{u}_{\text{adv}} = \frac{\overline{\mathbf{u}c}}{\bar{c}} \tag{8}$$

A correction factor is then applied $F_{\text{corr}} = \mathbf{u}_{\text{adv}}/\overline{\mathbf{u}}$ to convert $\overline{\mathbf{u}}$ into $\mathbf{u}_{\text{adv}}$. More details on calculating the correction factor can be found in Clare et al. (2021). The final form of the sediment concentration equation would then be:

$$\frac{\partial}{\partial t}(h\bar{c}) + \frac{\partial}{\partial x}\left(hF_{\text{corr}}\bar{u}_1\bar{c}\right) + \frac{\partial}{\partial y}\left(hF_{\text{corr}}\bar{u}_2\bar{c}\right)$$
$$= \frac{\partial}{\partial x}\left[h\left(c_s \frac{\partial \bar{c}}{\partial x}\right)\right] + \frac{\partial}{\partial y}\left[h\left(c_s \frac{\partial \bar{c}}{\partial y}\right)\right] + E_b - D_b \tag{9}$$

More in details about calculating the erosion and deposition terms can be found in Clare et al. (2021).

2.1. Bedload transport

For the bedload transport, we follow the equations developed in Tassi and Villaret (2014), where the bedload transport flux is calculated using the following equation:

$$\mathbf{Q_b} = \phi_s \sqrt{g\left(\frac{\rho_s}{\rho_f} - 1\right) d_{50}^3}(\cos \xi, \sin \xi) \tag{10}$$

where $\cos \xi = \frac{\bar{u}_1}{\sqrt{\bar{u}_1^2 + \bar{u}_2^2}}$ and $\sin \xi = \frac{\bar{u}_2}{\sqrt{\bar{u}_1^2 + \bar{u}_2^2}}$.

We choose the Meyer–Peter–Müller formula to define the non-dimensional sediment rate ϕ_s

$$\phi_s = \begin{cases} 0, & \theta' < \theta_{\text{cr}}, \\ \alpha_{\text{MPM}}\left(\theta' - \theta_{\text{cr}}\right)^{3/2}, & \text{otherwise}, \end{cases} \tag{11}$$

where d_{50} is the median sediment diameter, θ_{cr} is the critical shields parameter, α_{MPM} is a coefficient equal to 8 (Tassi and Villaret, 2014), and θ' the non-dimensional shields parameter having the following equation:

$$\theta' = \frac{\Psi \tau_b}{\left(\rho_s - \rho_f\right) g d_{50}} \tag{12}$$

where Ψ is the skin friction correction and τ_b is the bed shear stress acting against the velocity flow and equal in magnitude in both directions. For more details about the derivation of the former parameters, see Clare et al. (2021), Tassi and Villaret (2014).

2.1.1. Slope effect

In order to properly reflect the change in the magnitude and angle of water flow as the bed level changes, i.e gradient of the bed, we added a magnitude correction factor and an angle correction factor since they are not reflected in Eq. (10). Briefly, the effect of a downslope direction is to increase the bedload flux, while it reduces the transport flux in an upslope bedload direction.

1. *Magnitude correction of bedload transport:*
   The magnitude correction method is based on the Koch and Flokstra's formula (Koch and Flokstra, 1980) given by:

$$\mathbf{Q_{b*}} = \mathbf{Q_b}\left(1 - Y\frac{\partial z_b}{\partial s}\right) \tag{13}$$

where s is the direction tangential to the current and Y is an empirical factor having a default value of 1.3 (Tassi and Villaret, 2014). This correction tends to smooth results and reduce instabilities.

2. *Angle correction of bedload transport:*

The angle correction is taken into account by the following formula:

$$\tan \alpha = \tan \delta - T \frac{\partial z_b}{\partial n} \tag{14}$$

where α is the direction of solid transport with respect to the flow direction, δ is the direction of bottom shear stress with respect to the flow direction, and n is the coordinate along the axis perpendicular to the flow direction.

According to Talmon et al. (1995), the coefficient T is calculated as given below:

$$T = \frac{1}{\beta_2 \sqrt{\theta}} \tag{15}$$

where β_2 is an empirical coefficient, and θ is the Shields parameter (see Clare et al. (2021) for more details on the calculation of the Shields parameter).

2.2. New bed level

The final step in the model setup is to compute the new bed level, which is affected both suspended sediment and bedload transport, using Exner equation as follow:

$$\left(1 - p'\right) \frac{d z_b}{dt} + \nabla_h \cdot \mathbf{Q_b} = D_b - E_b \tag{16}$$

where p' is the bed sediment porosity.

2.3. Wet-dry domain

In a coastal simulation, there are three main domain types: (1) fully wet deep in the ocean, (2) wet-dry where water wets the domain over time, i.e at the beach, and (3) dry where water does not reach. However, since we are solving the nonlinear shallow water equations, the model might crash when simulating dry regions due to non-differentiability issues, like in very tall trees, which is why we decided to not include such regions in our simulations. Regarding the wet-dry domain, we decided to use a moving bathymetry, by including a wetting and drying parameter, that maintains a positive water depth without affecting the accuracy of the model (Kärnä et al., 2011; Donnelly et al., 2022). The modified total water depth is calculated in the following equation:

$$\tilde{h} := \eta - z_b + f(h), \tag{17}$$

where

$$f(h) := \frac{1}{2} \left(\sqrt{h^2 + \delta^2} - h \right), \tag{18}$$

with δ being the wetting and drying parameter discussed in Kärnä et al. (2011) who recommended to set it equal to

$$d \|\nabla h\|$$

where d is the length scale of the mesh. As a result of applying this modification, the hydrodynamic equations will become:

$$\frac{\partial \eta}{\partial t} + \nabla \cdot \left(\tilde{h}\overline{\mathbf{u}} \right) = 0, \tag{19}$$

$$\frac{\partial \overline{\mathbf{u}}}{\partial t} + \overline{\mathbf{u}} \cdot \nabla \overline{\mathbf{u}} - \nu \nabla^2 \overline{\mathbf{u}} + f \overline{\mathbf{u}}^\perp + g \nabla \eta = -\frac{\tau_b}{\rho \tilde{h}}. \tag{20}$$

In order to avoid non-differentiable functions, a numerical parameter ζ is added to the depth-averaged velocity:

$$\|\mathbf{u}\| \approx \sqrt{\|\mathbf{u}\|^2 + \zeta^2}, \tag{21}$$

where the value of ζ should be chosen adequately to avoid model crashes but not too large since this could leave to massive dissipation of the velocity due to friction. In our models, we have chosen a minimal value of 0.1 for the norm smoothing operator ζ. This ensures model differentiability and prevents model crashing while the effect on the friction term was kept minimal in such a way that it does not affect the velocity.

Furthermore, the sediment equation will be modified as follows:

$$\frac{\partial}{\partial t}(\tilde{h}\bar{c}) + \frac{\partial}{\partial x}\left(\tilde{h}F_{\text{corr}}\bar{u}_1\bar{c} \right) + \frac{\partial}{\partial y}\left(\tilde{h}F_{\text{corr}}\bar{u}_2\bar{c} \right) \tag{22}$$

$$= \frac{\partial}{\partial x}\left[\tilde{h}\left(c_s \frac{\partial \bar{c}}{\partial x} \right) \right] + \frac{\partial}{\partial y}\left[\tilde{h}\left(c_s \frac{\partial \bar{c}}{\partial y} \right) \right]$$

$$+ E_b - D_b$$

2.4. Hydro-morphodynamic application

2.4.1. Hydrodynamic spin-up

When simulating hydro-morphodynamics within Thetis, some instabilities could occur early on in the simulation since the water elevations might not have reached a stable state. To explain, when the simulation starts, the elevation and velocity fields are initially set to 0. Therefore, the transition to a quasi-steady state solution for elevation and velocity fields could trigger unrealistic bedlevel changes. Thus, as a common practice, we have initialised the simulation by first spinning-up the hydrodynamics (Gerritsen et al., 2008). Then, when these fields stabilise, morphodynamic equations will be introduced.

2.4.2. Morphological acceleration factor

Additionally, to decrease computational time, since changes in sediment morphology take a long time, a morphological acceleration factor is usually introduced (Morgan et al., 2020) to amplify those changes and save computational time. Applying that factor, m, to Exner equation:

$$\frac{\left(1 - p'\right)}{m} \frac{d z_b}{dt} + \nabla_h \cdot \mathbf{Q_b} = D_b - E_b. \tag{23}$$

The above equation means that at every time-step dt, the hydrodynamic and sediment change are equivalent to mdt.

3. Finite element discretisation

After defining the equations to be solved for the hydro-morphodynamic model, as discussed in Section 2, a discontinuous Galerkin-based (DG) finite element discretisation will be first developed for the aforementioned hydro-morphodynamic model and then implemented in *Thetis*, a finite element coastal ocean model built using the Firedrake code generating framework (Kärnä et al., 2018). The DG method was first proposed, for mathematical properties of the neutron transport equation, by Lesaint and Raviart in 1979 (Zienkiewicz et al., 2013). This method is proven to be robust for solving Navier Stokes problems (Fehn et al., 2018). In DG, an unstructured mesh is used where it is tessellated by triangular elements, and a finite element space is then defined on the mesh. The definition of the variables on a discontinuous space requires solving the variables on element edges with the union of the edges denoted by Γ. Thus, the average operator $\{\{.\}\}$ and jump operator $[[.]]$ across the interior on scalar and vector fields are defined below:

$$\{\{\mathbf{X}\}\} = \frac{1}{2} \left(\mathbf{X}^+ + \mathbf{X}^- \right) \tag{24}$$

$$[[\chi]]_{\mathbf{n}} = \chi^+ \mathbf{n}^+ + \chi^- \mathbf{n}^- \tag{25}$$

$$\lceil [\mathbf{X}]]_{\mathbf{n}} = \mathbf{X}^+ \cdot \mathbf{n}^+ + \mathbf{X}^- \cdot \mathbf{n}^- \tag{26}$$

where $\mathbf{n} = \left(n_x, n_y, 0 \right)$ is the horizontal projection of the outward pointing unit normal on the element edge, and "+ " and "-" denote

Fig. 1. Geographical location of the Sundarbans.

either side of the interior edge (Clare et al., 2021). The DG discretisation is actually similar to the finite volume method since it is local and fully conservative, yet with higher accuracy (Kärnä et al., 2018). Furthermore, this method has received lots of attention recently in hydro-morphodynamic applications since it is well suited for advection dominated problems and facilitates the use of unstructured meshes which are important for irregular geometries in coastal areas (Weinberg and Wieners, 2021)

A semi-implicit Crank–Nicolson time-stepping approach is applied since it is second order accurate and fast to run as it only needs one nonlinear solve per time-step. In addition, this time integrator approach does not dissipate tidal waves too much, and thus avoids having very smooth solutions (unlike the fully implicit backward Euler).

3.1. Sediment transport

In *Thetis*, an upwinding scheme is used in advection for sediment concentration $\bar{c}$ where at each edge, $\bar{c}$ is equal to the upstream value with respect to its velocity, $\bar{c}^{up}$. Thus, the weak form of the advection term $\bar{\mathbf{u}} \cdot \nabla_h \bar{c}$ in Eq. (9) can be given by:

$$\int_\Omega \psi \bar{\mathbf{u}} \cdot \nabla_h \bar{c} \, dx = -\int_\Omega \bar{c} \nabla_h \cdot (\bar{\mathbf{u}} \psi) dx + \int_\Gamma \bar{c}^{up} [[\psi \bar{\mathbf{u}}]]_\mathbf{n} ds \tag{27}$$

Where Ω is the tessellated domain.

Regarding the weak form of the diffusivity term, $-\nabla_h \cdot (c_s \nabla_h \bar{c})$, the Symmetric Interior Penalty Galerkin (SIPG) stabilisation method is applied to ensure stability with a penalty parameter, σ (see Kärnä et al. (2018) for more details). Hence, the weak form of the diffusivity term is:

$$-\int_\Omega \psi \nabla_h \cdot (\epsilon_s \nabla_h \bar{c}) \, dx$$
$$= \int_\Omega \epsilon_s (\nabla_h \psi) \cdot (\nabla_h \bar{c}) \, dx - \int_\Gamma [[\psi]]_\mathbf{n} \cdot \{\{\epsilon_s \nabla_h \bar{c}\}\} \, ds \tag{28}$$
$$- \int_\Gamma [[\bar{c}]]_\mathbf{n} \cdot \{\{\epsilon_s \nabla_h \psi\}\} \, ds + \int_\Gamma \sigma \{\{\epsilon_s\}\} [[\bar{c}]]_\mathbf{n} \cdot [[\psi]]_\mathbf{n} ds$$

Finally, the weak form of the erosion and deposition term, $E_b - D_b$, is given as:

$$\int_\Omega (\text{Source Term}) \psi \, dx = \int_\Omega (E_b - D_b) \psi \, dx \tag{29}$$

Applying Crank–Nicolson time integrator, the final equation would be:

$$\int_\Omega \frac{\bar{c}_i^{(n+1)} - \bar{c}_i^{(n)}}{\Delta t} \psi \, dx = (1 - \Theta)(F_i^{(n+1)} + F_i^n) \tag{30}$$

where F_i^{n+1} is the sum of the weak forms given in Eqs. (27),(28),(29) and $\Theta = 0.5$. Note that for forward Euler, $\Theta = 0$ and for a backward Euler, $\Theta = 1$. This is commonly known as the "Theta scheme" (Mbehou, 2018).

3.2. Exner equation

According to Clare et al. (2021), to avoid unstable solutions when solving the Exner equation, as discussed in Section 2.2, the bedlevel, z_b, is defined on a continuous grid, and a continuous Galerkin (CG) discretisation space is used to project the hydrodynamic and sediment transport variables from the DG space. The weak form of the divergence term, $\nabla_h \cdot \mathbf{Q_b}$, in Eq. (16) is then given below:

$$\int_\Omega \psi \nabla_h \cdot \mathbf{Q_b} dx = -\int_{d\Omega} (\mathbf{Q_b} \cdot \mathbf{n}) \psi \, ds + \int_\Omega (\mathbf{Q_b} \cdot \nabla_h) \psi \, dx \tag{31}$$

Applying Crank–Nicolson, Eq. (16) is solved as follow:

$$\int_\Omega \left((1 - p') \frac{z_{b_i}^{(n+1)} - z_{b_i}^{(n)}}{\Delta t} \right) \psi \, dx = (1 - \Theta)(G_i^{(n+1)} + G_i^n) \tag{32}$$

where $G_i^{(n+1)}$ is the sum of Eqs. (29) and (33).

4. Case study location: Sundarbans

The Sundarbans is the largest single tract mangrove forest in the world with an area covering 10,000 km^2 distributed between Bangladesh (60%) and India (40%). The water elevation at the Sundarbans varies between 0.5 m and 3 m with 70% of the region under 1 m (Mukul et al., 2019). The Sundarbans region is adversely affected by extreme climatic events, particularly tropical cyclones, the frequency and intensity of which is increasing in a warming world. This has added pressure on the mangrove environments where a recent study showed that the mangrove extent decreased from 2307 km^2 in 1968 to 1851 km^2 in
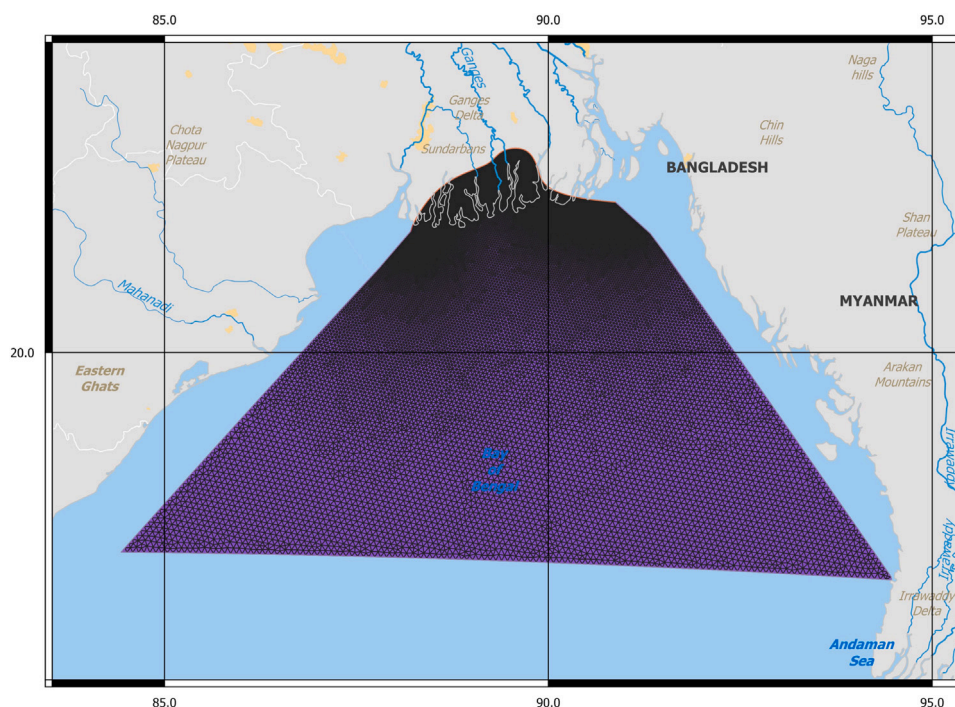
Fig. 2. Mesh generated using Gmsh with varying resolution from 1.5 km to 8 km.

2016, and linear extrapolation of the current trends suggests that the extent could further reduce to 1376–1470 km² by 2066 (Sievers et al., 2020).

4.1. Computational domain

The modelled region covers the entire shelf of the Bay of Bengal in addition to the entire Sundarbans mangrove forest spanning both India and Bangladesh, as shown in Fig. 1.

A mesh generation domain, *qmesh* (Avdis et al., 2018), and the mesh generation tool, *Gmsh* (Geuzaine and Remacle, 2009) were employed to produce an unstructured mesh covering the area of interest with varying mesh resolution from 1.5 km at the Sundarbans to 8 km at the southern boundary of the Bay of Bengal. The generated mesh is shown in Fig. 2.

The bathymetry of the region was obtained from satellite imagery data from the General Bathymetric Chart of the Oceans (GEBCO) (Lemenkova, 2020) which has a resolution of about 15 arc seconds and is suitable for our region, which has a maximum length of about 570 km and a maximum width of about 1070 km. The maximum depth reached at the modelled region of the Bay of Bengal is about 2685 m while the maximum elevation of modelled mangrove trees is about 8 m. Note that some trees have a height of more than 20 m, however, since the maximum tidal elevation reached at the bay of Bengal is about 4 m, the model would reach some instabilities when modelling these dry regions. To further explain our reasoning behind this idea, modelling dry regions is not trivial, especially, for hydro-morphodynamics. To remedy this issue, one could set a very large wetting and drying parameter so that the model accounts for any dry region. However, this would lead to too much wave inundation thus neglecting the effect of the mangroves in dissipating waves and resulting in inaccurate results. As a result, we chose a smaller value for the wetting and drying parameter, 2, in order to consider the full effect of mangrove environments on incoming waves which is the main aim of our study. This will not affect the numerical simulation results in any way as the unreached wave heights are considered a fully dry region which is not affected by the waves. Thus, a maximum elevation of 8 m was selected in this model to ensure that this height is well enough to

Table 2
Classification of land use type and their respective Manning's coefficient.

Land use type	Manning's coefficient
Open water/sand	0.02
Scattered brush/shrub/scrub	0.05 (0.035 to 0.07)
Forest/estuarine forested wetland	0.10 (0.08 to 0.12)
Dense woods (e.g. dense willows)	0.15 (0.11 to 0.20)

cover any incoming wave extent and height, but at the same time will avoid the model to unnecessarily to crash. Fig. 3 shows the bathymetry of the region.

The major tidal harmonic constituents at the Bay of Bengal are M_2, S_2, N_2, K_1, and O_1 (Sindhu and Unnikrishnan, 2013). However, to improve the accuracy of the numerical model, additional tidal constituents were added such as M_4, M_f, P_1, Q_1, K_2, and $2N_2$. These harmonic constituents were used to generate tidal waves at the sea boundary of the region from the TPXO tidal harmonic database (Egbert and Erofeeva, 2002). No boundary conditions were imposed at the mangrove land boundary in order to examine the full effect of the incoming waves in terms of inundation and wave height reach.

The simulated periods followed those by Sindhu and Unnikrishnan (2013), which will be used as a validation for the results presented in this paper, that were from 20 June 1981 to 30 September 1981. The spin-up period was ten days for the model with mangrove trees and the model without mangrove trees; and the time-step was 12 s. More details will be found in Section 5.

In order to simulate the complex bathymetry and interactions between the waves and mangrove environments, several spatially varying parameters were introduced such as the Manning coefficient, bed height, and viscosity. In McIvor et al. (2012), Manning's coefficient for mangrove environments was determined as 0.15 which represents a dense forest. Table 2 shows the difference between Manning's coefficient for different forest environments.

As the water depth increases, Manning's coefficient was set to be the same as seabed. To determine Manning's coefficient for seabed, a fine sand bed was assumed which gives a Manning's value of about 0.012 according to the British Geological Survey bed classification (Mackie
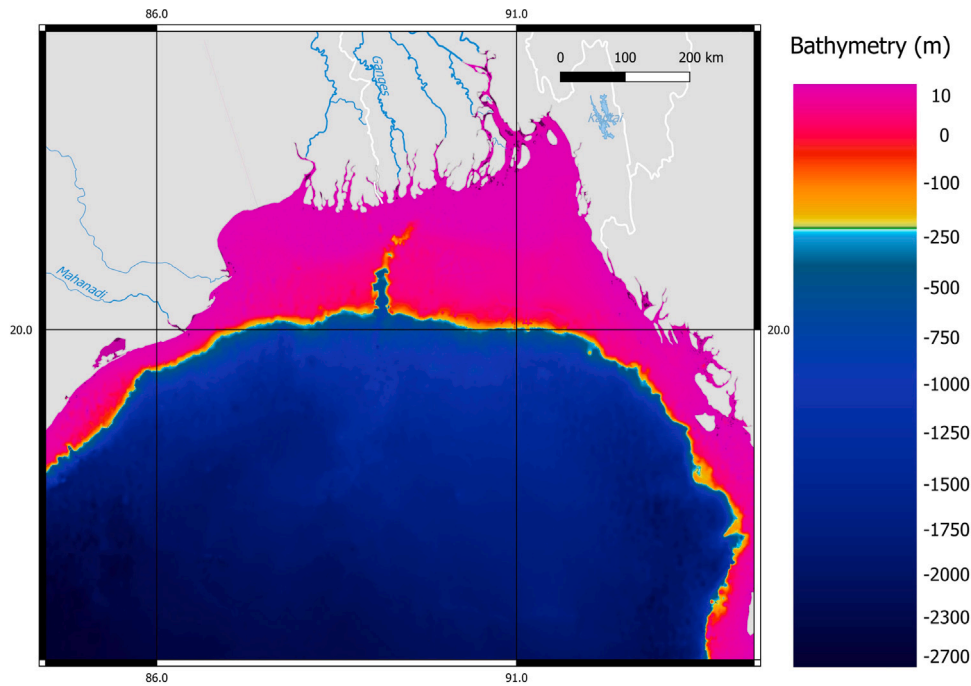
Fig. 3. Bathymetry of the modelled region.

Table 3
British Geological Survey bed classification and associated grain size observations subsequently applied in calculating roughness length and Manning coefficient.

Bed classification	d_{50} (mm)	z_0 (mm)	n $\left(\text{sm}^{-1/3}\right)$
Bedrock	$768 \leq d_{50} < 2048$	$64.00 \leq z_0 < 170.7$	$0.045 \leq n < 0.053$
Boulder	$256 \leq d_{50} < 768$	$21.33 \leq z_0 < 64.00$	$0.037 \leq n < 0.045$
Cobble	$64 \leq d_{50} < 256$	$5.333 \leq z_0 < 21.33$	$0.029 \leq n < 0.037$
Very coarse gravel	$32 \leq d_{50} < 64$	$2.667 \leq z_0 < 5.333$	$0.026 \leq n < 0.029$
Coarse gravel	$16 \leq d_{50} < 32$	$1.333 \leq z_0 < 2.667$	$0.023 \leq n < 0.026$
Medium gravel	$8 \leq d_{50} < 16$	$0.667 \leq z_0 < 1.333$	$0.021 \leq n < 0.023$
Fine gravel	$4 \leq d_{50} < 8$	$0.333 \leq z_0 < 0.667$	$0.019 \leq n < 0.021$
Very coarse sand	$2 \leq d_{50} < 4$	$0.167 \leq z_0 < 0.333$	$0.017 \leq n < 0.019$
Coarse sand	$1 \leq d_{50} < 2$	$0.083 \leq z_0 < 0.167$	$0.015 \leq n < 0.017$
Medium sand	$0.5 \leq d_{50} < 1$	$0.042 \leq z_0 < 0.083$	$0.013 \leq n < 0.015$
Fine sand	$0.25 \leq d_{50} < 0.5$	$0.021 \leq z_0 < 0.042$	$0.012 \leq n < 0.013$
Very fine sand	$0.125 \leq d_{50} < 0.25$	$0.010 \leq z_0 < 0.021$	$0.010 \leq n < 0.012$
Silt, clay, mud	$0.0625 \leq d_{50} < 0.125$	$0.005 \leq z_0 < 0.010$	$0.009 \leq n < 0.010$

Table 4
Parameter values distribution according to varying depth.

y-coordinate	Manning's coefficient n $(\text{sm}^{-1/3})$	Bed height m	Horizontal viscosity v $(\text{m}^2\ \text{s}^{-1})$
$2.5 \times 10^6 < y < 2.4 \times 10^6$	0.15	0.25	1500
$2.4 \times 10^6 < y < 2.35 \times 10^6$	0.012	0.5	500
$2.35 \times 10^6 < y < 2.25 \times 10^6$	0.002	3	80
$2.25 \times 10^6 < y < 2 \times 10^6$	0.0015	20	300
$y > 2 \times 10^6$	0.001	30	48

et al., 2021). For very deep water levels, friction becomes negligible and tidal elevations are insensitive to the friction coefficient (Sindhu and Unnikrishnan, 2013). Table 3 shows the distribution of Manning's coefficient according to different sediment sizes.

The effect of changing viscosity is minimal in such large regions (Sindhu and Unnikrishnan, 2013), and they are mostly used for calibration purposes (Li and Huang, 2013), where suitable values for these parameters follow this equation:

$$v = \delta_x * U, \tag{33}$$

where δ_x is the mesh element size and U is a suitable velocity metric (typically tidal current). Finally, bed height was adjusted to reflect the depth of the region where at the coast, bed height was minimal and increased with increasing depth. In Sindhu and Unnikrishnan (2013), the same mesh element size of 9.5 km × 9.5 km was used, and after sensitivity analysis, the horizontal eddy viscosity was set at 1500 m²/s as it achieved the best agreement between observed and simulated elevations.

5. Results

After building the hydro-morphodynamic model using the equations discussed in Sections 2 and 3, we demonstrate the effectiveness and accuracy of the proposed model on quantifying the ability of mangrove environments to attenuate waves and prevent erosion. To address that subject, two different experiments were conducted: one with mangrove environments and the other without them. Note that in all cases, the morphological acceleration factor was set at 50.

5.1. Experiment 1: With mangroves

As discussed in Section 4, some spatially varying parameters were introduced to properly simulate the effect of mangrove environments on wave attenuation and sediment stabilisation. Table 4 shows the variation of Manning's coefficient, bed height, and horizontal viscosity as a function of increasing depth using y-coordinate values. Note that viscosity values varied, unlike in Sindhu and Unnikrishnan (2013), since in the mesh resolution in this paper varied from 1.5 km to 8 km as was mentioned previously in 4.1.

The time step was set at 12 s, and the mesh resolution increased from 8 km at the sea boundary to 1.5 km at the Sundarbans, which is suitable for such large domain used in this study. The boundary conditions used were already mentioned in details in Section 4. Fig. 4 shows the state of the region after the hydrodynamic spin-up. It can be noticed that the Sundarbans region had almost no water elevation.
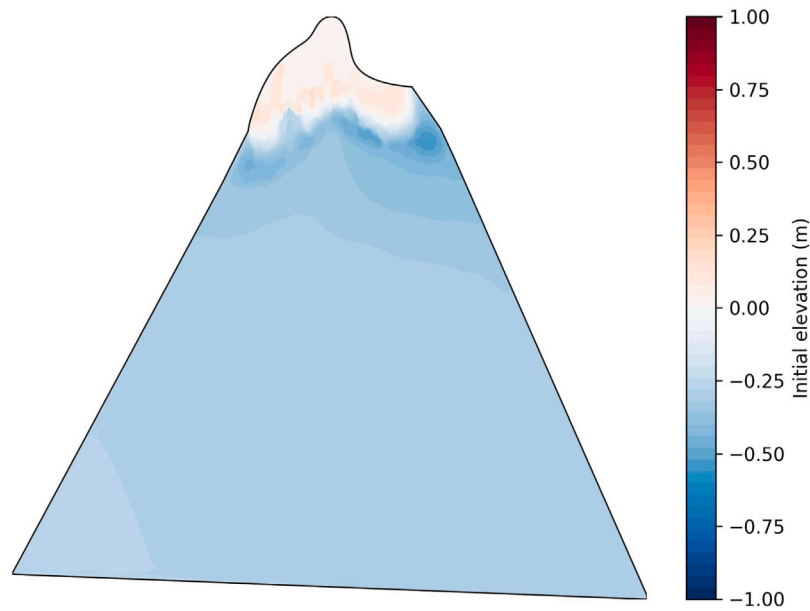
Fig. 4. Initial elevation of the region after hydrodynamic spin-up.

Fig. 5 shows the change in water elevation, velocity, and seabed evolution across the modelled domain at peak (left-hand column) and end of tide (right-hand column). From Figs. 5(a) and 5(b), the tidal waves propagate from the Bay of Bengal at the southern boundary to reach the Sundarbans mangrove forest at the northern boundary. At the peak of the tide, wave heights reached a maximum value of about 1.2 m, which is just before hitting the mangrove environments. Once entered the Sundarbans, Fig. 5(b) shows how water elevation quickly dissipates and the waves are attenuated. At the end of the cycle, most water elevation had been attenuated, and water goes back to 0.03 m representing a 97.5% wave attenuation caused by the friction generated from mangrove environments. As a result, water propagation deep in the mangrove environment is minimal, where Figs. 5(c) and 5(d) show how the depth-averaged velocity magnitude decreases from about 0.45 m/s before hitting the mangroves to 0.01 m/s after hitting the mangroves, which is equivalent to a 97.7% decrease in water velocity.

Regarding sediment erosion, negligible sediment change was observed from Figs. 5(e) and 5(f), especially at the Sundarbans region, due to the low water velocity at that region which is not significant enough to move sediment particles and the complex root structure of mangrove environments which stabilises the bed and prevent any erosion.

5.2. Experiment 2: Without mangroves

In the other experiment, mangrove trees were removed by replacing the height of those trees with 0 m and decreasing Manning's coefficient in this region to a value of 0.0025 $sm^{-1/3}$ similar to Sindhu and Unnikrishnan (2013). The bed reference height and horizontal viscosity were kept the same as the previous experiment.

Fig. 6 shows the change in elevation, velocity, and seabed for this case study at peak (left-hand column) and end of tide (right-hand column). Here, the changes in all fields are much more significant than the previous experiment. Figs. 6(a) and 6(b) show that tidal heights reached a maximum height of more than 2 m at peak tide and 1.55 m at the land boundary of the region at the end of the tide.

From Fig. 6(d), the depth-averaged velocity magnitude reached 2.7 m/s at the land boundary which indicates the capability of water to go beyond the modelled region and further inundate more land regions, which could endanger human lives in the immediate vicinity.

Most significantly, sediment erosion is now clearly visible in this region, especially where the mangrove environment was previously present, which is evident as shown in Figs. 6(e) and 6(f). Such results show the dangers this region could be in without the presence of mangrove environments, and particularly if faced with an extreme climate event such as a cyclone.

For comparing the results obtained from the two experiments discussed above, we subtracted the elevation, velocity, and seabed fields for the peak and end of tide simulations. Fig. 7 shows the results of the differences between the previous experiments for all fields.

Figs. 7(a) and 7(b) show how significant the wave heights differences are between the experiments with and without mangroves. The height difference reached around 0.7 m at peak tide and more than 1 m at end of tide due to the absence of mangrove environments. This observation is also similar for both velocity and bedlevel changes.

From these results, we can conclude that mangrove environments are able to attenuate waves heights and velocities by more than 98%, and prevent almost entirely any sediment erosion when compared to the same region without mangroves. This highlights the effectiveness of mangrove environments in protecting the coast and preventing any further inundation of water coming from the sea.

We have also included results of one full tidal cycle for the elevation (Figs. A.12 & A.14) and bedlevel changes (Figs. A.13 & A.15) for the experiments with and without mangroves in Appendix.

5.3. Experiment 3: Comparing with experiment 1 - sensitivity analysis

In this section, we performed a sensitivity analysis test to evaluate the impact of different values of the friction factors on the model's performance with the similar conditions and parameters used in Sindhu and Unnikrishnan (2013). The main difference between this experiment and the previous ones is mostly in changing horizontal viscosity to be constant at 1500 m^2/s and Manning's friction according to the following criteria:

$$n = 0.12 \text{ for } y \leq 2.5 \times 10^6$$
$$n = 0.002 \text{ for } 2.5 \times 10^6 < y \leq 2.42 \times 10^6 \quad (34)$$
$$n = 0.0015 \text{ for } y < 2.42 \times 10^6.$$

Note that the main purpose of decreasing Manning's friction factor at the mangrove environments was also to investigate the effect of decreasing the friction factor under the assumption that the mangrove environments would follow a forest/estuarine forested wetland land type instead of dense woods as shown in Table 2.
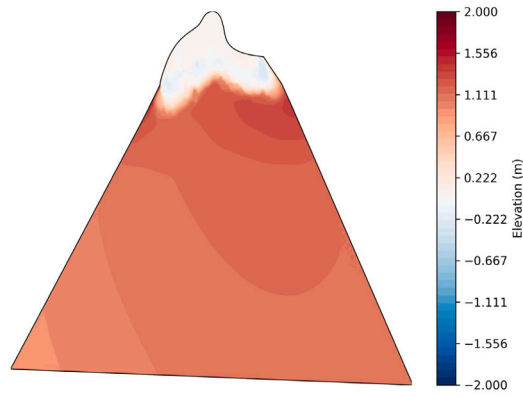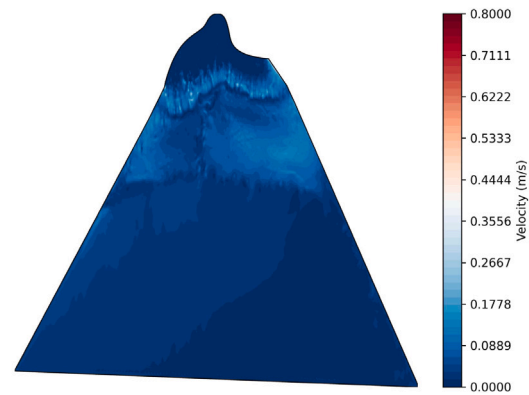
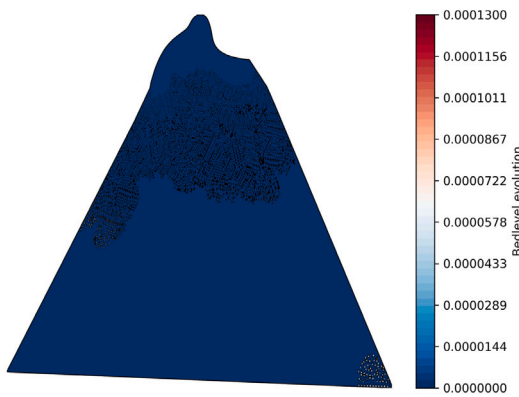(a) Elevation for mangrove experiment at peak tide
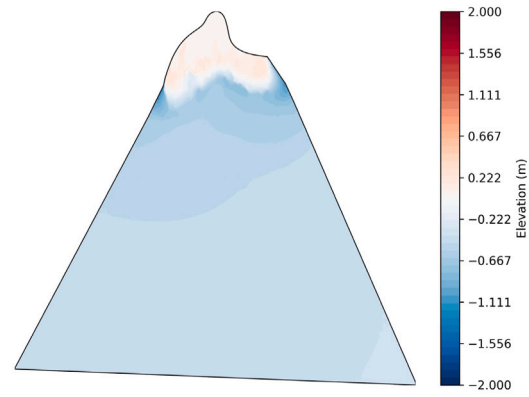
(b) Elevation for mangrove experiment at end of tide
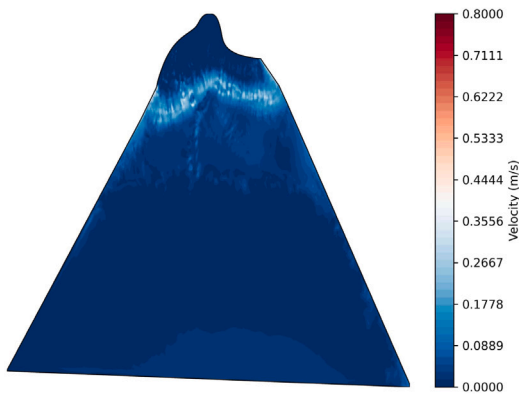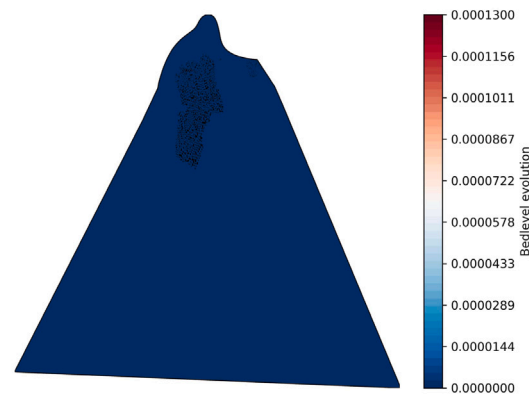

(c) Velocity for mangrove experiment at peak tide

(d) Velocity for mangrove experiment at end of tide

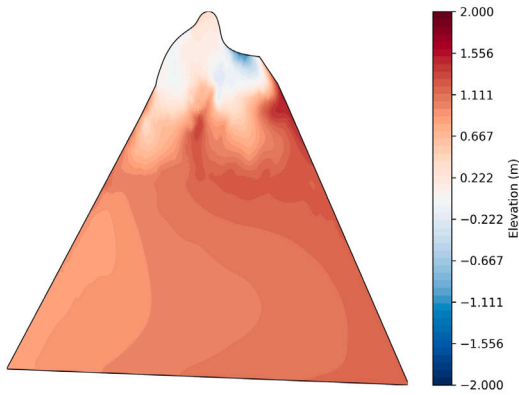(e) Bedlevel evolution for mangrove experiment at peak tide

(f) Bedlevel evolution for mangrove experiment at end of tide

**Fig. 5.** Simulation results for mangrove experiment.

Fig. 8 shows the change in elevation, velocity, and bedlevel for this experiment. From Figs. 8(a) and 8(b), it can be noticed that water elevation reached similar heights, about 1 m, when compared with experiment 1 before decreasing to 0.03 m after encountered mangrove environments. Similarly, the depth-average velocity magnitude decreased from 0.45 m/s to 0.002 m/s beyond the mangroves as shown in Figs. 8(c) and 8(d). Finally, the profile of the seabed at peak tide and at the end of the tide, shown in Figs. 8(a) and 8(e) is very similar to that in experiment 1.

This experiment shows the effect of having such a large horizontal viscosity value on water elevation since the former acts as a sponge that leads to the dissipation of wave heights. This effect is visible mainly

(a) Elevation for the experiment without mangroves at peak tide
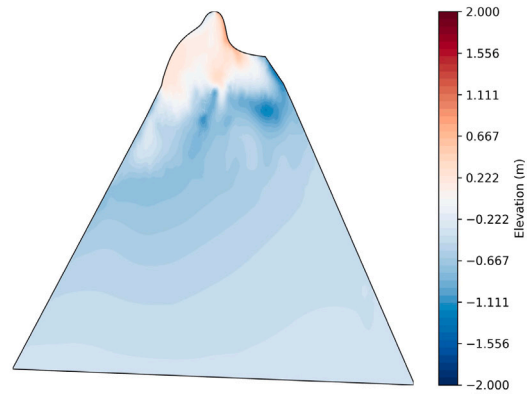
(b) Elevation for the experiment without mangroves at end of tide
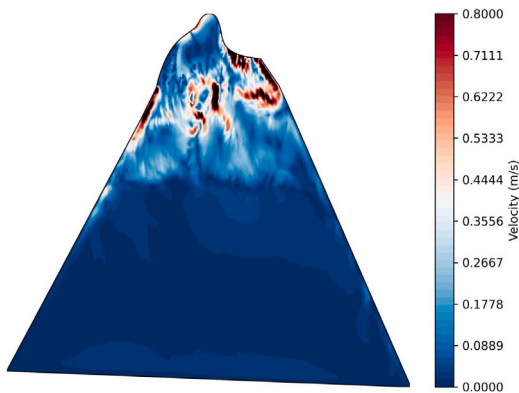
(c) Velocity for the experiment without mangroves at peak tide
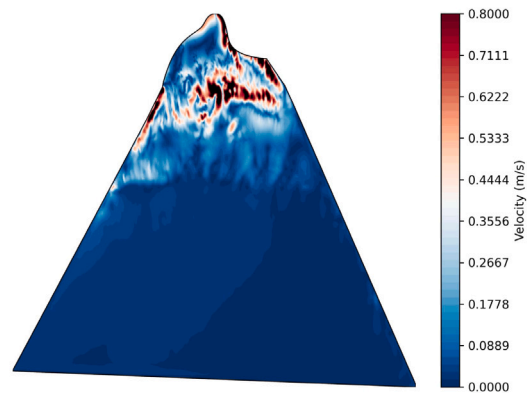
(d) Velocity for the experiment without mangroves at end of tide
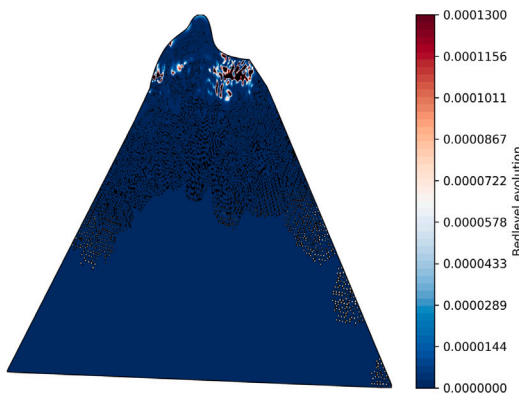
(e) Bedlevel evolution for the experiment without mangroves at peak tide
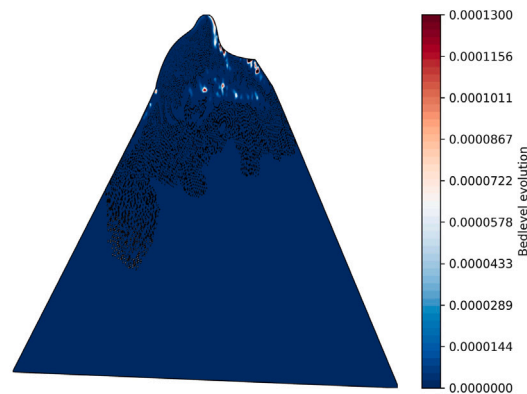
(f) Bedlevel evolution for the experiment without mangroves at end of tide

Fig. 6. Simulation results for the experiment without mangroves.

at the mangrove environments where water velocity was much less than that in experiment 1; however, in very deep regions, the effect of viscosity is negligible. In addition, the effect of decreasing Manning's friction was not observed (since it would have been expected to see increase in water elevations after decreasing friction) which could be

due to the large area of mangrove environments in this region (about 76 km in length and 145 km in width) that will dissipate most of the wave energy reaching to the end of the region.

Fig. 9 compares elevation, velocity, and bedlevel differences between Experiments 3 and 1 at both peak and end of tide cycles. The
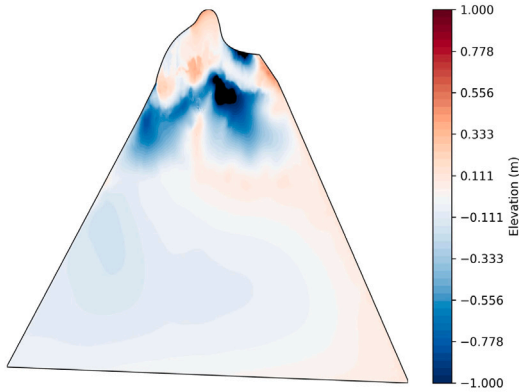
(a) Elevation difference between experiments with and without mangroves at peak tide
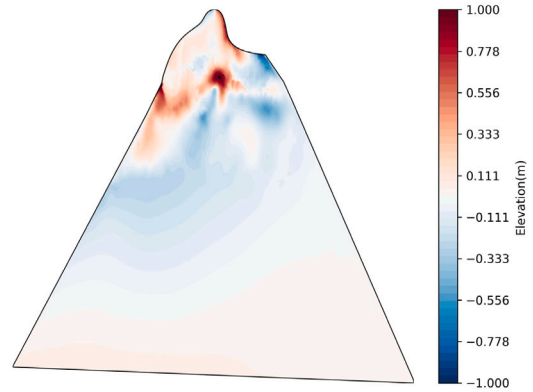
(b) Elevation difference between experiments with and without mangroves at end of tide
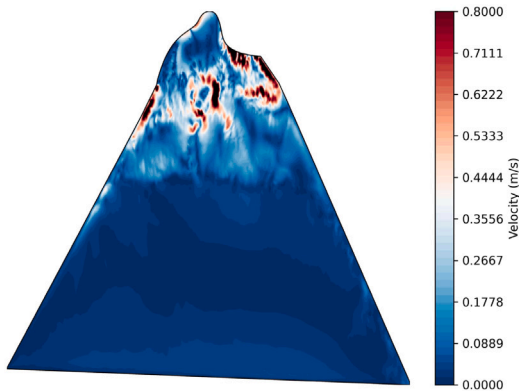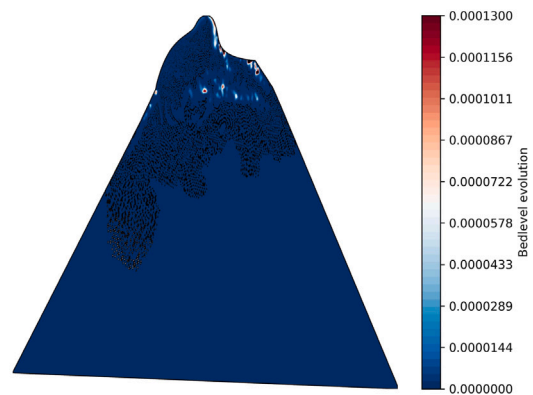
(c) Velocity difference between the experiments at peak tide
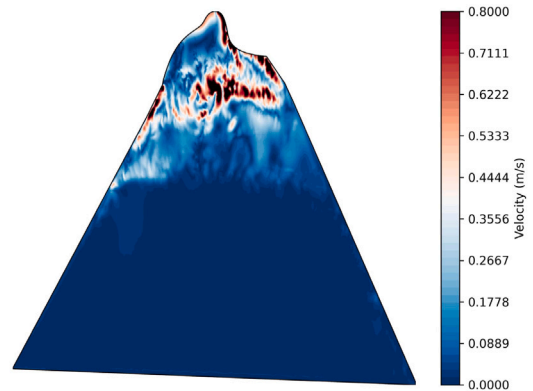
(d) Velocity difference between the experiments at end of tide
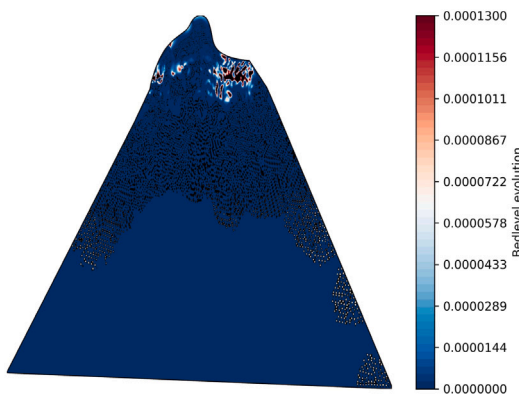
(e) Bedlevel difference between the experiments at peak tide

(f) Bedlevel difference between the experiments at end of tide

Fig. 7. Difference between experiments with and without mangroves at peak tide and at end of tide.

differences shown in this figure confirm the previous analysis of changing the Manning's parameter as the differences are almost negligible.

Thus, it is concluded that our model obtained similar results between the defined conditions and the conditions from the other experiment.
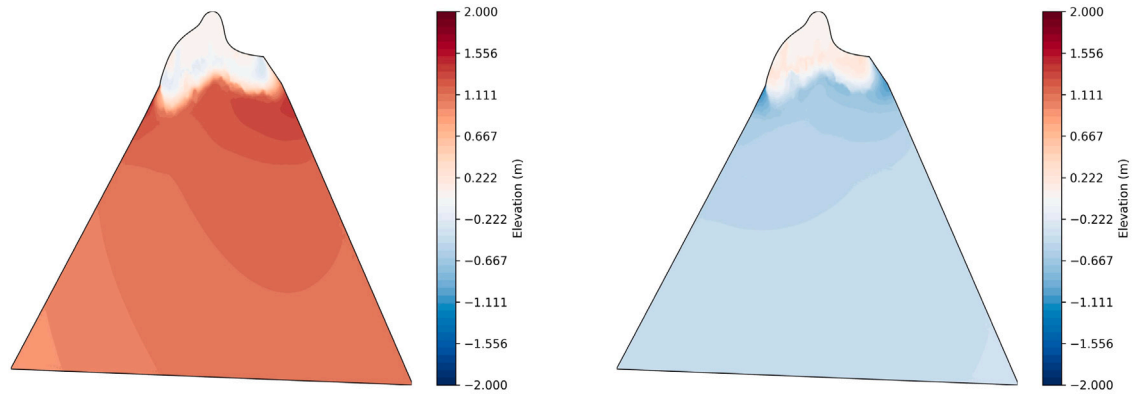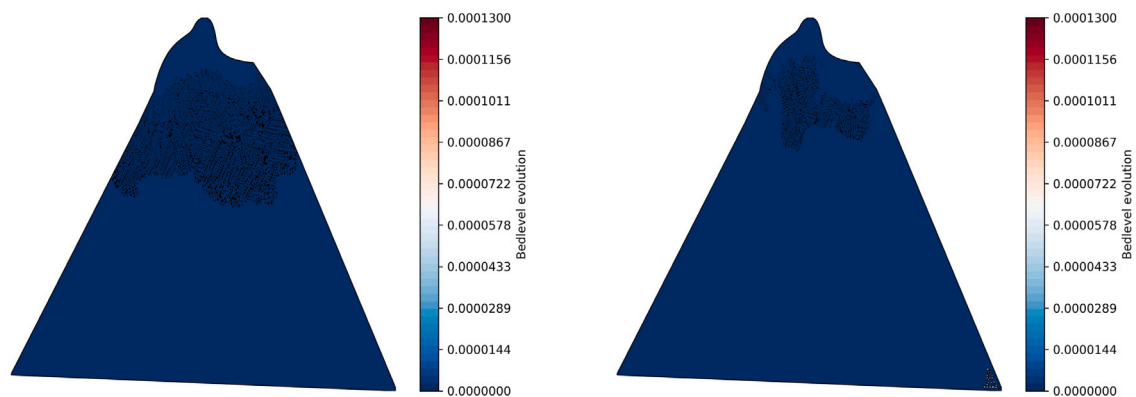
(a) Elevation for sensitivity experiment at peak tide

(b) Elevation for sensitivity experiment at end of tide
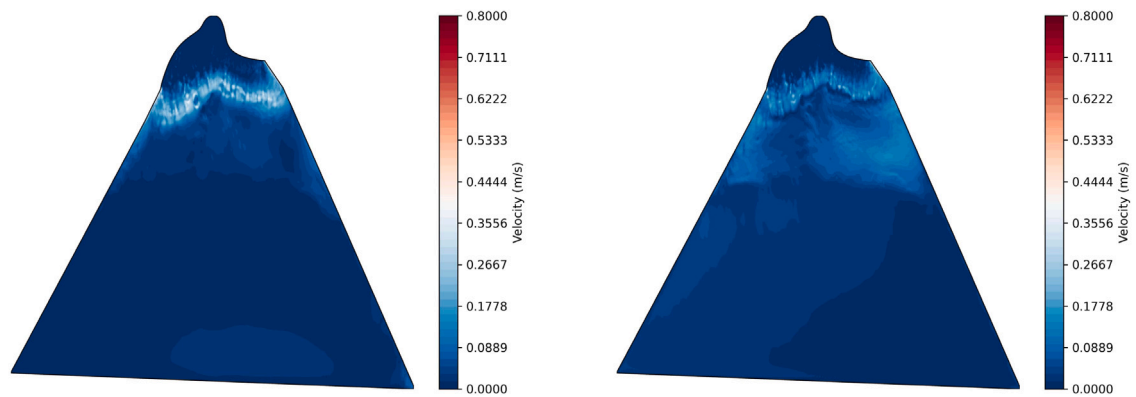
(c) Velocity for sensitivity experiment at peak tide

(d) Velocity for sensitivity experiment at end of tide

(e) Bedlevel evolution for sensitivity experiment at peak tide

(f) Bedlevel evolution for sensitivity experiment at end of tide

**Fig. 8.** Simulation results for sensitivity experiment.

6. Model validation: Comparing with Sindhu and Unnikrishnan (2013) and tidal gauge data

In Sindhu and Unnikrishnan (2013), the authors compared the performance of their developed model with some data available from tidal stations, namely Paradip, Visakhapatnam, and Chennai. However,

since none of these stations are included in our domain, we decided to increase the domain in order to cover Paradip tidal station. Fig. 10 shows the newly created domain which covers Paradip tidal station, and thus it will be used for validating our model's performance with the model from Sindhu and Unnikrishnan (2013) and the tidal data from that station. On a side note, the main reason behind not selecting
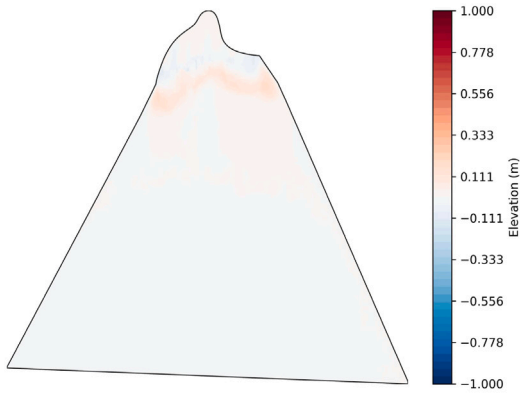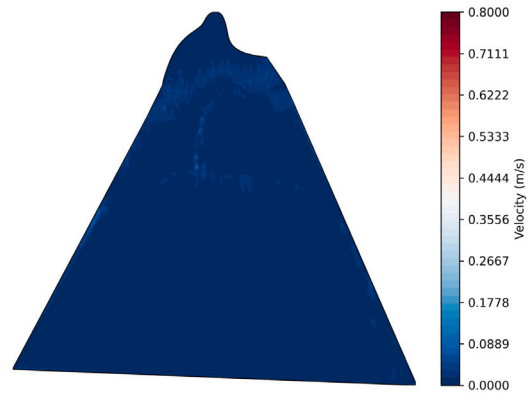
(a) Elevation difference between sensitivity and mangrove experiments at peak tide
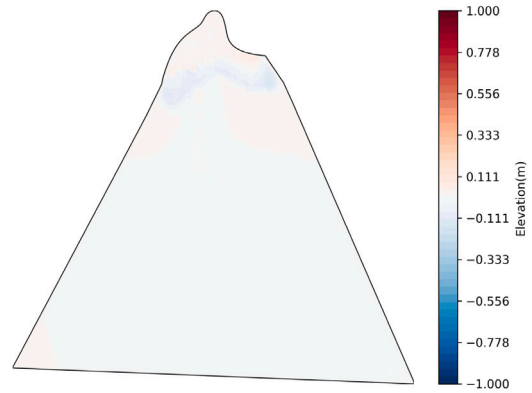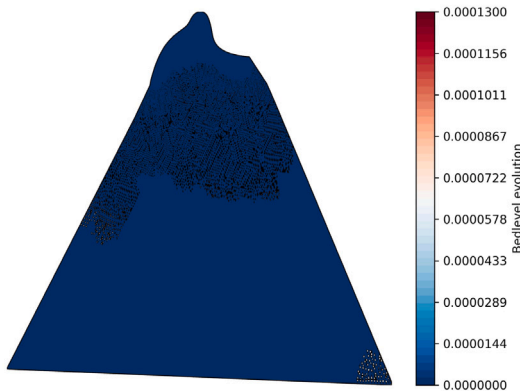

(b) Elevation difference between sensitivity and mangrove experiments at end of tide
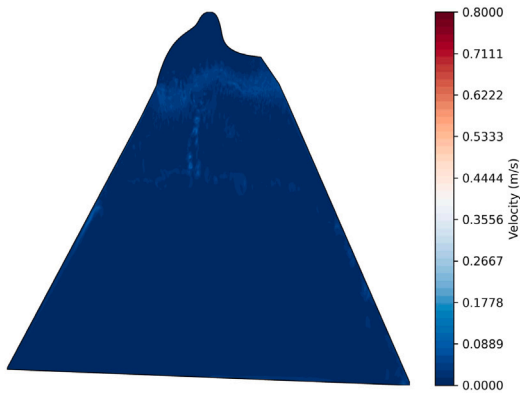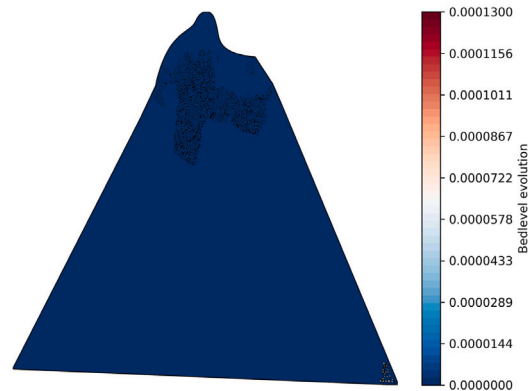

(c) Velocity difference between sensitivity and mangrove experiments at peak tide

(d) Velocity difference between sensitivity and mangrove experiments at end of tide

(e) Bedlevel difference between sensitivity and mangrove experiments at peak tide

(f) Bedlevel difference between sensitivity and mangrove experiments at end of tide

Fig. 9. Difference between sensitivity and mangrove experiments at peak tide and at end of tide.
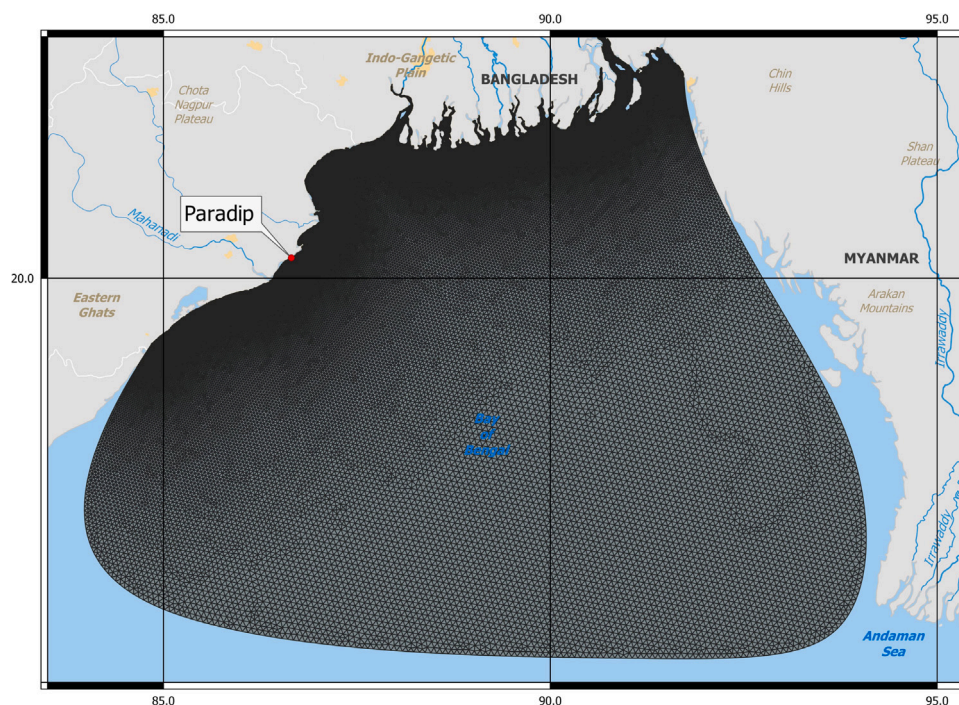
Fig. 10. New domain created to extend towards Paradip tidal station.

this domain for all above experiments was to avoid very long simulation times as the current benchmarking experiment took about two weeks to complete. In addition, the wetting and drying parameter was removed as this experiment is not modelling mangroves anymore but just the tidal elevations at Paradip.

Due to the lack of data available from both the other experiment and Paradip for 1981, it was decided to choose another year with climatically similar conditions to 1981. To achieve this criteria, the Dipole Mode Index (DMI) was selected as a reference for climatically similar years. The DMI is an indicator for temperature change from East to West across the tropical Indian Ocean (McPhaden and Nagura, 2013). It measures the strength of the Indian Ocean Dipole (IOD) which is an indicator of climate variability in the Indian Ocean. Both 1981 and 2013 had negative DMI values for August with 1981 having 6 consecutive months with negative DMI values (June–November) while 2013 had eight consecutive months with negative DMI values (February–September) according to the NOAA extended reconstructed sea surface temperature V5 dataset. In addition, the 6-month running mean DMI of 1981 was −0.2 and the 8-month running mean for 2013 was −0.182. As a result, 2013 was chosen as a reference for a climatically similar year to 1981. In addition, the tidal data for Paradip for August 2013 is available, thus we ran the simulation for the whole month of August 2013 and plotted the results against the tidal data of that station.

Fig. 11 shows the simulated water elevations at the selected region after adjusting the data to mean-sea level which is 1.66 m (Sindhu and Unnikrishnan, 2013).

The obtained results show that our model is capable at simulating the modelled region accurately where very similar wave structures and wave heights were obtained in comparison with the tidal station. The maximum achieved tidal heights of the numerical model was 1.16 m vs 1.2 m for the observed data for a total error of 3.3%, whereas both the simulated and observed minimum tidal data were 1 m. On the other hand, the model in Sindhu and Unnikrishnan (2013) overestimated the peak tide height by over 10 cm (7.2% error). It is important to note the slight differences between the simulated and observed data at the beginning of the simulation. Although the model had a 10 day spin-up period to stabilise its hydrodynamics, more time should have been given for the spinning period due to the large domain modelled in this

experiment. Other reasons to justify the differences between the observed and simulated could be the presence of complex geometry near the station which is not properly modelled in the numerical simulation. The sensitivity of the global tidal model to the bathymetry, especially to steep depth change where diffusivity is maximum, could be another reason. Finally, increasing mesh resolution would also improve the accuracy of the model but at the expense of time.

Nonetheless, we believe that our model is suitable and produces valuable results since it uses a more accurate numerical scheme (finite element discontinuous Galerkin vs finite difference scheme), a better global tidal solver, TPXO, which solves for both elevation and velocity with more tidal harmonics unlike the used model, FES2004, that just solves for elevation, and has a higher mesh resolution than the other model.

7. Conclusions and outlook

This study is a first-time application of a coupled hydro-morphodynamic model using discontinuous Galerkin finite element discretisation for a real-world case using next-generation coastal ocean models like Thetis. The Sundarbans, the largest mangrove forest in the world, was taken as a case study, as it is one of the most threatened mangrove environments due to the threat of multiple severe climate events across the region. By presenting magnitude and angle correction factors for bedload transport, adding a wet-dry parameter/domain to avoid numerical instabilities, using spatially varying parameters, and spinning-up the hydrodynamics, the developed model showed the importance of mangrove environments in attenuating waves and preventing erosion. These environments reduced wave heights by more than 97% and prevented any erosion when compared with the same region but without mangroves.

We validated the performance of our model by comparing its simulation results with another model i.e., Sindhu and Unnikrishnan (2013) in accurately estimating water elevation at a specific tidal gauge. Our model showed better accuracy with an error of 3.3% in comparison to 7.2% when estimating peak tidal heights. However, this region lacked multiple in-situ hourly data of water levels over the Bay of Bengal. Nonetheless, it would be beneficial to check and refine the findings
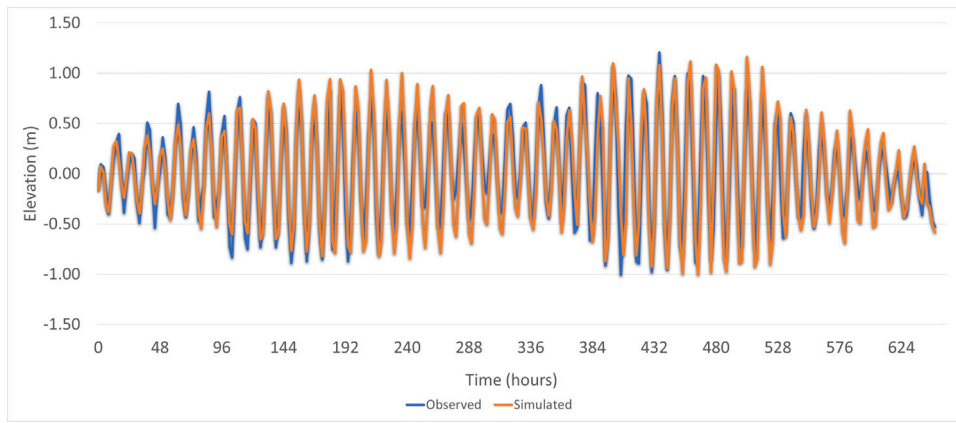
Fig. 11. Comparison of simulated tidal elevation (m with respect to chart datum) with the observed tidal elevation obtained from tide gauge records at Paradip August 2013.
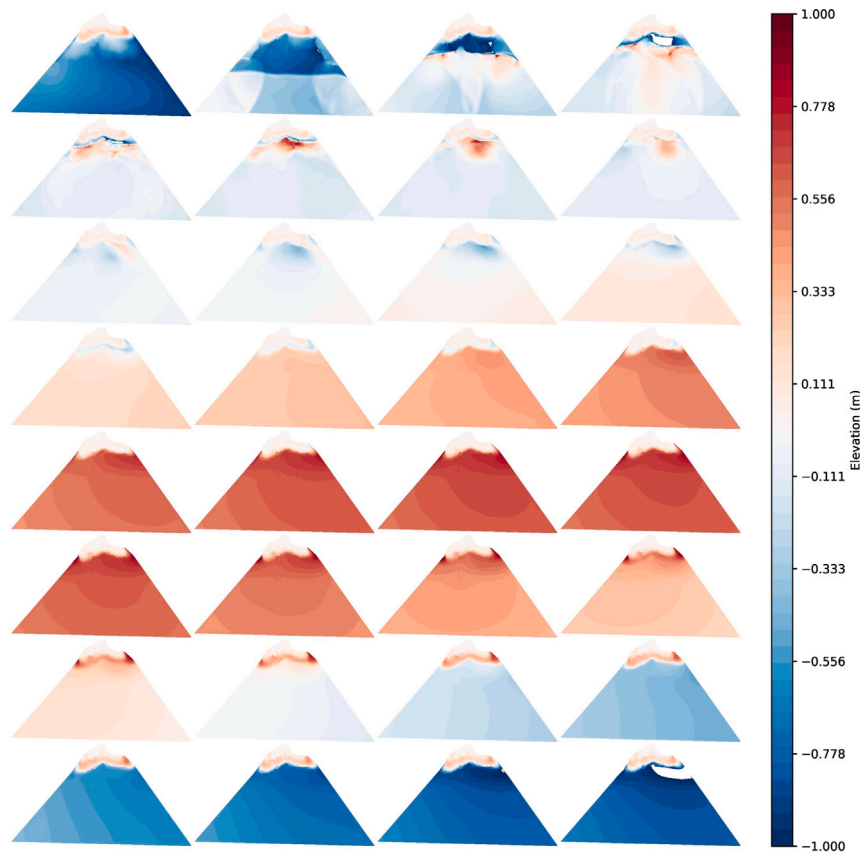

Fig. A.12. Tidal height changes for the experiment with mangroves.

reported in the present study, when data from more tidal stations become available for the simulated years.

On the other hand, and since this model is developed by solving the depth-averaged Navier Stokes, two main limitations arise. First, the assumptions made in this model are not translated to quantified uncertainty in the output, which is due to the nature of Navier Stokes' solution as it is just a mathematical model. Second, the time taken to spin-up the hydrodynamics and then to model the morphodynamics is quite significant as the former accounts to 25 h and the later to about 10 h, with the morphological acceleration factor of 50, rising to 20 days without the acceleration. This high computational time would limit the benefits of using such numerical models, especially when continuous monitoring of the environment is required as in a mangrove restoration project.

A possible solution to the aforementioned limitations would be to use machine learning models in two possible scenarios: (a) as a full surrogate where the results of the numerical model would be used as an input and output data to the machine learning model, and the latter would have to figure a relationship between the input and the output; (b) as a physics-informed model which requires much less amounts of data from the numerical model since prior knowledge, in the form of boundary and initial conditions, would be used as a penalty/loss term to help the model converge accurately to the output. In either way, such models would possibly have much faster predictions than the numerical model solutions, and an uncertainty quantification method could be added to better understand the confidence of the model with unobserved data.
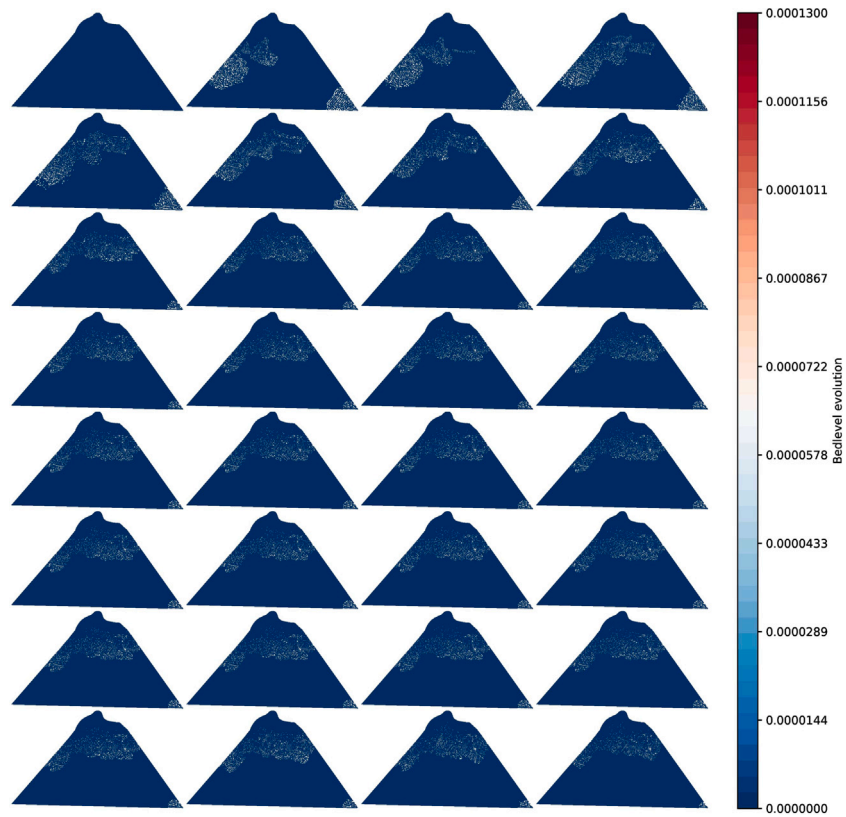
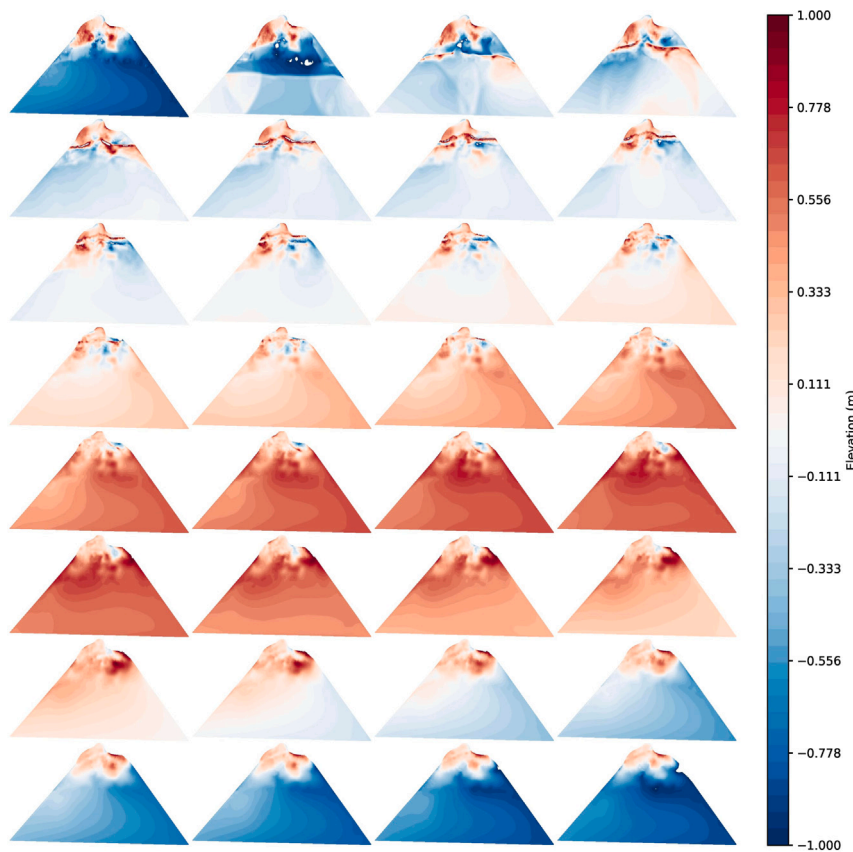**Fig. A.13.** Bedlevel changes for the experiment with mangroves.

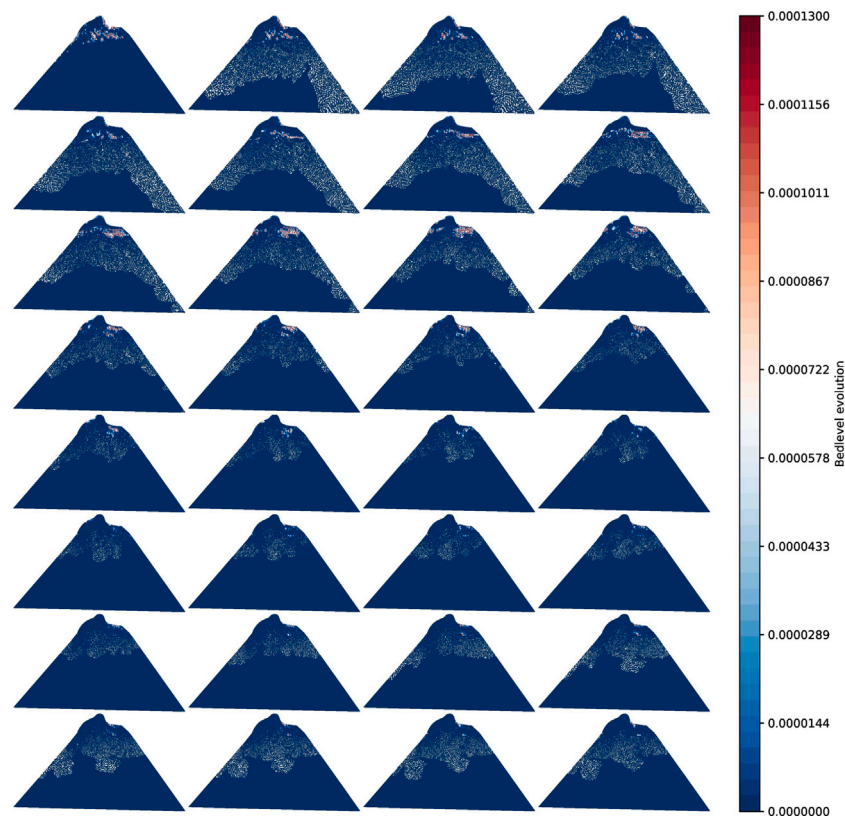**Fig. A.14.** Tidal height changes for the experiment without mangroves.

Fig. A.15. Bedlevel changes for the experiment without mangroves.

CRediT authorship contribution statement

Majdi Fanous: Conceptualisation, Software, Experimental design, Writing – original draft. **Alireza Daneshkhah:** Conceptualisation, Methodology, Writing – review & editing, Project administration, Funding acquisition. **Jonathan M. Eden:** Conceptualisation, Writing – review & editing, Supervision. **Renji Remesan:** Validation, Data curation. **Vasile Palade:** Writing – review & editing, Supervision.

Declaration of competing interest

The authors declare that they have no known competing financial interests or personal relationships that could have appeared to influence the work reported in this paper.

Data availability

Data will be made available on request.

Acknowledgements

Appendix

The figures in this section show a full tidal cycle evolution for the elevation and bedlevel for the experiments with and without mangroves. For each figure, the cycle goes from top to bottom and from left to right.

References

Alvarez, E.A., Rico-Secades, M., Suárez, D.F., Gutiérrez-Trashorras, A.J., Fernández-Francos, J., 2016. Obtaining energy from tidal microturbines: A practical example in the Nalón River. Appl. Energy 183, 100–112. http://dx.doi.org/10.1016/J.APENERGY.2016.08.173.

Avdis, A., Candy, A.S., Hill, J., Kramer, S.C., Piggott, M.D., 2018. Efficient unstructured mesh generation for marine renewable energy applications. Renew. Energy 116, 842–856. http://dx.doi.org/10.1016/J.RENENE.2017.09.058.

Bolle, A., Mercelis, P., Roelvink, D., Haerens, P., Trouw, K., 2010. Application and validation of XBEACH for three different field sites. Coast. Eng. Proc. 1 (32), 40. http://dx.doi.org/10.9753/ICCE.V32.SEDIMENT.40, URL: https://icce-ojs-tamu.tdl.org/icce/index.php/icce/article/view/1247.

Brand, E., Chen, M., Montreuil, A.L., 2020. Optimizing measurements of sediment transport in the intertidal zone. Earth-Sci. Rev. 200, 103029. http://dx.doi.org/10.1016/J.EARSCIREV.2019.103029.

Cannon, D., Kibler, K., Donnelly, M., McClenachan, G., Walters, L., Roddenberry, A., Phagan, J., 2020. Hydrodynamic habitat thresholds for mangrove vegetation on the shorelines of a microtidal estuarine lagoon. Ecol. Eng. 158, 106070. http://dx.doi.org/10.1016/J.ECOLENG.2020.106070.

Castillo, P., Gómez, S., 2021. Conservative local discontinuous Galerkin methods for a generalized system of strongly coupled nonlinear Schrödinger equations. Commun. Nonlinear Sci. Numer. Simul. 99, 105836. http://dx.doi.org/10.1016/J.CNSNS.2021.105836.

Clare, M.C., Percival, J.R., Angeloudis, A., Cotter, C.J., Piggott, M.D., 2021. Hydro-morphodynamics 2D modelling using a discontinuous Galerkin discretisation. Comput. Geosci. 146, 104658. http://dx.doi.org/10.1016/J.CAGEO.2020.104658.

Donnelly, J., Abolfathi, S., Pearson, J., Chatrabgoun, O., Daneshkhah, A., 2022. Gaussian process emulation of spatio-temporal outputs of a 2D inland flood model. Water Res. 225, 119100.

Egbert, G.D., Erofeeva, S.Y., 2002. Efficient inverse modeling of barotropic ocean tides. J. Atmos. Ocean. Technol. 19 (2), 183–204. http://dx.doi.org/10.1175/1520-0426(2002)019<0183:EIMOBO>2.0.CO;2, URL: https://journals.ametsoc.org/view/journals/atot/19/2/1520-0426_2002_019_0183_eimobo_2_0_co_2.xml.

Erduran, K.S., Kutija, V., 2003. Quasi-three-dimensional numerical model for flow through flexible, rigid, submerged and non-submerged vegetation. J. Hydroinform. 5 (3), 189–202. http://dx.doi.org/10.2166/HYDRO.2003.0015, URL: http://iwaponline.com/jh/article-pdf/5/3/189/392584/189.pdf.

Fehn, N., Wall, W.A., Kronbichler, M., 2018. Robust and efficient discontinuous Galerkin methods for under-resolved turbulent incompressible flows. J. Comput.

Phys. 372, 667–693. http://dx.doi.org/10.1016/J.JCP.2018.06.037, arXiv:1801.08103.

Gerritsen, H., de Goede, E., Platzek, F., van Kester, J., Genseberger, M., Uittenbogaard, R., 2008. Validation document Delft3D-flow; a software system for 3D flow simulations.

Geuzaine, C., Remacle, J.F., 2009. Gmsh: A 3-D finite element mesh generator with built-in pre- and post-processing facilities. Internat. J. Numer. Methods Engrg. 79 (11), 1309–1331. http://dx.doi.org/10.1002/NME.2579, https://onlinelibrary.wiley.com/doi/full/10.1002/nme.2579, https://onlinelibrary.wiley.com/doi/abs/10.1002/nme.2579, https://onlinelibrary.wiley.com/doi/10.1002/nme.2579.

Harris, C.K., Traykovski, P.A., Geyer, W.R., 2005. Flood dispersal and deposition by near-bed gravitational sediment flows and oceanographic transport: A numerical modeling study of the Eel River shelf, northern California. J. Geophys. Res.: Oceans 110 (C9), 1–16. http://dx.doi.org/10.1029/2004JC002727, https://onlinelibrary.wiley.com/doi/full/10.1029/2004JC002727, https://onlinelibrary.wiley.com/doi/abs/10.1029/2004JC002727, https://agupubs.onlinelibrary.wiley.com/doi/10.1029/2004JC002727.

Huybrechts, N., Villaret, C., Hervouet, J.M., 2010. Comparison between 2D and 3D modelling of sediment transport: application to the dune evolution. In: River Flow 2010. Karlsruhe, pp. 887–894, URL: http://henry.baw.de/handle/20.500.11970/99731.

Kärnä, T., de Brye, B., Gourgue, O., Lambrechts, J., Comblen, R., Legat, V., Deleersnijder, E., 2011. A fully implicit wetting–drying method for DG-FEM shallow water models, with an application to the Scheldt Estuary. Comput. Methods Appl. Mech. Engrg. 200 (5–8), 509–524. http://dx.doi.org/10.1016/J.CMA.2010.07.001.

Kärnä, T., Kramer, S.C., Mitchell, L., Ham, D.A., Piggott, M.D., Baptista, A.M., 2018. Thetis coastal ocean model: Discontinuous Galerkin discretization for the three-dimensional hydrostatic equations. Geosci. Model Dev. 11 (11), 4359–4382. http://dx.doi.org/10.5194/GMD-11-4359-2018, arXiv:1711.08552.

Kennedy, A.B., Chen, Q., Kirby, J.T., Dalrymple, R.A., 2000. Boussinesq modeling of wave transformation, breaking, and Runup.I: 1D. J. Waterw. Port Coast. Ocean Eng. 126 (1), 39–47. http://dx.doi.org/10.1061/(ASCE)0733-950X(2000)126:1(39), https://ascelibrary.org/doi/abs/10.1061/%28ASCE%290733-950X%282000%29126%3A1%2839%29, https://ascelibrary.org/doi/10.1061/%28ASCE%290733-950X%282000%29126%3A1%2839%29.

Koch, F., Flokstra, C., 1980. Bed Level Computations for Curved Alluvial Channels. Delft Hydraulics Laboratory, Delft [Netherlands].

Le Minor, M., Bartzke, G., Zimmer, M., Gillis, L., Helfer, V., Huhn, K., 2019. Numerical modelling of hydraulics and sediment dynamics around mangrove seedlings: Implications for mangrove establishment and reforestation. Estuar. Coast. Shelf Sci. 217, 81–95. http://dx.doi.org/10.1016/J.ECSS.2018.10.019.

Lemenkova, P., 2020. Gebco gridded bathymetric datasets for mapping Japan trench geomorphology by means of GMT scripting toolset. Geod. Cartogr. (Vilnius) 46 (3), 98–112. http://dx.doi.org/10.3846/GAC.2020.11524.

Li, L., Huang, Z., 2013. Modeling the Change of Beach Profile Under Tsunami Waves: A Comparison of Selected Sediment Transport Models, Vol. 7, No. 1. World Scientific Publishing Company, http://dx.doi.org/10.1142/S1793431113500012.

Luettich, Jr., R., Westerink, J., 2004. Formulation and numerical implementation of the 2D/3D ADCIRC finite element model version 44.XX.

Lynett, P., Liu, P., Sitanggang, K., Kim, D.H., 2004. Modeling Wave Generation Evolution and Interaction with Depth-Integrated Dispersive Wave Equations COULWAVE Code Manual. Technical Report.

Ma, G., Shi, F., Kirby, J.T., 2012. Shock-capturing non-hydrostatic model for fully dispersive surface wave processes. Ocean Model. 43–44, 22–35. http://dx.doi.org/10.1016/J.OCEMOD.2011.12.002.

Mackie, L., Evans, P.S., Harrold, M.J., O'Doherty, T., Piggott, M.D., Angeloudis, A., 2021. Modelling an energetic tidal strait: investigating implications of common numerical configuration choices. Appl. Ocean Res. 108, 102494. http://dx.doi.org/10.1016/J.APOR.2020.102494.

Masson-Delmote, V., Zhai, P., Pirani, A., Connors, S., Pean, C., Berger, S., Caud, N., Chen, Y., Goldfarb, L., Gomis, M., Huang, M., Leitzell, K., Lonnoy, E., Matthews, J., Maycock, T., Waterfield, T., Yelekci, O., Yu, R., Zhou, B., 2022. IPCC, 2022: Climate Change 2022: Impacts, Adaptation and Vulnerability. Contribution of Working Group II to the Sixth Assessment Report of the Intergovernmental Panel on Climate Change. Technical Report, Cambridge University.

Mbehou, M., 2018. The theta-Galerkin finite element method for coupled systems resulting from microsensor thermistor problems. Math. Methods Appl. Sci. 41 (4), 1480–1491. http://dx.doi.org/10.1002/MMA.4678, https://onlinelibrary.wiley.com/doi/full/10.1002/mma.4678, https://onlinelibrary.wiley.com/doi/abs/10.1002/mma.4678, https://onlinelibrary.wiley.com/doi/10.1002/mma.4678.

McIvor, A., Spencer, T., Möller, I., Spalding, M., 2012. Storm surge reduction by mangroves. In: The Nature Conservancy and Wetlands International. Technical Report, University of Cambridge, p. 36, URL: https://repository.tudelft.nl/islandora/object/uuid:79fe752e-ce52-4bf6-a45c-2847bead07ab?collection=research.

McPhaden, M.J., Nagura, M., 2013. Indian ocean dipole interpreted in terms of recharge oscillator theory. Clim. Dyn. 42 (5), 1569–1586. http://dx.doi.org/10.1007/S00382-013-1765-1, URL: https://link.springer.com/article/10.1007/s00382-013-1765-1.

Morgan, J.A., Kumar, N., Horner-Devine, A.R., Ahrendt, S., Istanbullouglu, E., Bandaragoda, C., 2020. The use of a morphological acceleration factor in the simulation of large-scale fluvial morphodynamics. Geomorphology 356, 107088. http://dx.doi.org/10.1016/J.GEOMORPH.2020.107088.

Mukul, S.A., Alamgir, M., Sohel, M.S.I., Pert, P.L., Herbohn, J., Turton, S.M., Khan, M.S.I., Munim, S.A., Reza, A.H., Laurance, W.F., 2019. Combined effects of climate change and sea-level rise project dramatic habitat loss of the globally endangered Bengal tiger in the Bangladesh Sundarbans. Sci. Total Environ. 663, 830–840. http://dx.doi.org/10.1016/J.SCITOTENV.2019.01.383.

Ou, S.H., Liau, J.M., Hsu, T.W., Tzang, S.Y., 2002. Simulating typhoon waves by SWAN wave model in coastal waters of Taiwan. Ocean Eng. 29 (8), 947–971. http://dx.doi.org/10.1016/S0029-8018(01)00049-X.

Peng, S.H., 2012. 1D and 2D numerical modeling for solving dam-break flow problems using finite volume method. J. Appl. Math. 2012, http://dx.doi.org/10.1155/2012/489269.

Prastica, R.M.S., 2018. Employing Galerkin method and field study for model calibration to perform sediment transport modelling in Agathis Lake, Universitas Indonesia. AIP Conf. Proc. 2014 (1), 020070. http://dx.doi.org/10.1063/1.5054474, URL: https://aip.scitation.org/doi/abs/10.1063/1.5054474.

Purohit, A., Vaidya, M., Chavan, K., Kudale, M., 2015. Effect of mega bridge on hydro – morphodynamics of waterfront facilities in wide estuarine harbours- A sustainable development. Aquati. Procedia 4, 341–348. http://dx.doi.org/10.1016/J.AQPRO.2015.02.046.

Ringler, T., Petersen, M., Higdon, R.L., Jacobsen, D., Jones, P.W., Maltrud, M., 2013. A multi-resolution approach to global ocean modeling. Ocean Model. 69, 211–232. http://dx.doi.org/10.1016/J.OCEMOD.2013.04.010.

Shchepetkin, A.F., McWilliams, J.C., 2003. A method for computing horizontal pressure-gradient force in an oceanic model with a nonaligned vertical coordinate. J. Geophys. Res.: Oceans 108 (C3), 3090. http://dx.doi.org/10.1029/2001JC001047, https://onlinelibrary.wiley.com/doi/full/10.1029/2001JC001047, https://onlinelibrary.wiley.com/doi/abs/10.1029/2001JC001047, https://agupubs.onlinelibrary.wiley.com/doi/10.1029/2001JC001047.

Sholichin, M., Prayogo, T.B., Bisri, M., Andrei, A., Robert, B., Erika, B., 2017. Numerical limitations of 1D hydraulic models using MIKE11 or HEC-RAS software – Case study of Baraolt river, Romania. IOP Conf. Ser.: Mater. Sci. Eng. 245 (7), 072010. http://dx.doi.org/10.1088/1757-899X/245/7/072010, https://iopscience.iop.org/article/10.1088/1757-899X/245/7/072010, https://iopscience.iop.org/article/10.1088/1757-899X/245/7/072010/meta.

Shu, C.W., Tan, S., 2017. Inverse Lax–Wendroff procedure for numerical boundary treatment of hyperbolic equations. Handb. Numer. Anal. 18, 23–52. http://dx.doi.org/10.1016/BS.HNA.2016.10.001.

Sievers, M., Chowdhury, M.R., Adame, M.F., Bhadury, P., Bhargava, R., Buelow, C., Friess, D.A., Ghosh, A., Hayes, M.A., McClure, E.C., Pearson, R.M., Turschwell, M.P., Worthington, T.A., Connolly, R.M., 2020. Indian Sundarbans mangrove forest considered endangered under Red List of Ecosystems, but there is cause for optimism. Biol. Cons. 251, 108751. http://dx.doi.org/10.1016/J.BIOCON.2020.108751.

Sindhu, B., Unnikrishnan, A.S., 2013. Characteristics of Tides in the Bay of Bengal, Vol. 36, No. 4. Taylor & Francis Group, pp. 377–407. http://dx.doi.org/10.1080/01490419.2013.781088, URL: https://www.tandfonline.com/doi/abs/10.1080/01490419.2013.781088.

Talmon, A., Struiksma, N., Mierlo, M.V., 1995. Laboratory measurements of the direction of sediment transport on transverse alluvial-bed slopes. J. Hydraul. Res. 33 (4), 495–517. http://dx.doi.org/10.1080/00221689509498657.

Tassi, P., Villaret, C., 2014. Finite Volume Methods for Hyperbolic Problems. Cambridge University Press, p. 558, URL: https://usermanual.wiki/Pdf/sisypheusermanualenv6p3.856450291/html.

Tavakkol, S., Lynett, P., 2020. Celeris Base: An interactive and immersive Boussinesq-type nearshore wave simulation software. Comput. Phys. Comm. 248, 106966. http://dx.doi.org/10.1016/J.CPC.2019.106966.

Tolkova, E., 2014. Land–water boundary treatment for a tsunami model with dimensional splitting. Pure Appl. Geophys. 171 (9), 2289–2314. http://dx.doi.org/10.1007/S00024-014-0825-8, URL: https://link.springer.com/article/10.1007/s00024-014-0825-8.

Villaret, C., Hervouet, J.M., Kopmann, R., Merkel, U., Davies, A.G., 2013. Morphodynamic modeling using the Telemac finite-element system. Comput. Geosci. 53, 105–113. http://dx.doi.org/10.1016/J.CAGEO.2011.10.004.

Wahid, S.M., Babel, M.S., Bhuiyan, A.R., 2007. Hydrologic monitoring and analysis in the Sundarbans mangrove ecosystem, Bangladesh. J. Hydrol. 332 (3–4), 381–395. http://dx.doi.org/10.1016/J.JHYDROL.2006.07.016.

Waldman, S., Bastón, S., Nemalidinne, R., Chatzirodou, A., Venugopal, V., Side, J., 2017. Implementation of tidal turbines in MIKE 3 and Delft3D models of Pentland Firth & Orkney Waters. Ocean & Coastal Management 147, 21–36. http://dx.doi.org/10.1016/J.OCECOAMAN.2017.04.015.

Warner, J.C., Sherwood, C.R., Signell, R.P., Harris, C.K., Arango, H.G., 2008. Development of a three-dimensional, regional, coupled wave, current, and sediment-transport model. Comput. Geosci. 34 (10), 1284–1306. http://dx.doi.org/10.1016/J.CAGEO.2008.02.012.

Warren, I.R., Bach, H.K., 1992. MIKE 21: a modelling system for estuaries, coastal waters and seas. Environ. Softw. 7 (4), 229–240. http://dx.doi.org/10.1016/0266-9838(92)90006-P.

Weinberg, K., Wieners, C., 2021. Dynamic phase-field fracture with a first-order discontinuous Galerkin method for elastic waves. Comput. Methods Appl. Mech. Engrg. 389, http://dx.doi.org/10.1016/j.cma.2021.114330, arXiv:2106.15193v2.

World Meteorological Organization, 2021. Greenhouse gas bulletin: Another year another record. URL: https://public.wmo.int/en/media/press-release/greenhouse-gas-bulletin-another-year-another-record.

Zienkiewicz, O., Taylor, R., Zhu, J., 2013. Multidomain mixed approximations. In: The Finite Element Method: Its Basis and Fundamentals. Butterworth-Heinemann, pp. 361–378. http://dx.doi.org/10.1016/B978-1-85617-633-0.00011-3.